# Low Temperature Epitaxial Growth of III-Nitride Semiconductors on Silicon Carbide Templates by Remote Plasma Metal-Organic Chemical Vapor Deposition

Robert Dubreuil

**Presented to the faculty of Electrical and Computer Engineering in partial fulfillment for a M.Sc. degree**

Lakehead University

Thunder Bay, Ontario

December 2017

# Abstract

Group III-Nitride (III-N) semiconductors are of high interest due to their thermal and electrical properties. Opposed to other III-V group semiconductors III-N semiconductors are hexagonal wurtzite structures that have a direct bandgap across the entire composition range. This wide bandgap range covers from the deep ultra-violet to the infrared region of the electromagnetic spectrum. This makes the III-N semiconductor group ideal for LEDs, laser diodes and photodetectors.

This thesis presents an in-depth study to the growth of III-Nitrides on Silicon Carbide (SiC) templates. Due to the difficulty in growing bulk crystals for the III-Nitrides, non-native substrates must be used. Because of this, there exists a lattice mismatch between the substrates and thin films grown on top. SiC proves to be an ideal substrate as the lattice mismatch is around 3.5%. Thin films of III-N were grown upon commercially purchased SiC templates using remote plasma enhanced metal organic chemical vapor deposition (RP-MOCVD) in the Lakehead University Semiconductor Research Lab. Results were characterized using x-ray diffraction (XRD), atomic force microscope (AFM), Energy-dispersive X-ray spectroscopy (EDX) and Ramen spectroscopy.

# Table of Contents

# List of Figures

# List of Acronyms

Metal Organic Chemical Vapour Deposition (MOCVD)
Silicon Carbide (SiC)
Gallium Nitride (GaN)
Aluminum Nitride (AlN)
Indium Nitride (InN)
Indium Gallium Nitride (InGaN)
Aluminum Gallium Nitride (AlGaN)
Indium Aluminum Nitride (InAlN)
Light Emitting Diode (LED)
High Electron Mobility Transistors (HEMT)
Two-Dimensional Electron Gas (2DEG)
Coefficient of Thermal Expansion (CTE)
Molecular Beam Epitaxy (MBE)
Atomic Layer Deposition (ALD)
Full Width at Half Maximum (FWHM)
Residual Gas Analyzer (RGA)
Metal Organic (MO)
Liner Combination of Atomic Orbitals (LCAO)

# Chapter 1 Introduction

## 1.1 Thesis Outline

Chapter one serves as a summarization of the historical growths of the group III-Nitrides along with the motivation for this dissertation. Chapter two covers all the materials of interest from each of the III-V Nitrides along with the SiC substrate used for this research. Chapter three looks at the measurement techniques used to qualify the results and to provide a quick background in each technique for further analysis later in this work. Chapter four outlines a theoretical MOCVD reactor in a typical industrial application including growth mechanics using both traditional growing techniques and plasma enhanced MOCVD. Chapter four then continues to the reactor currently in use at Lakehead University in the Semiconductor Research Lab. Chapter five contains a summarization of the research done. Chapter six covers some theoretical calculations concerning the band structure and of the effect of impurities upon the band structure using the LCAO technique. Chapter seven summarizes all work done in this thesis and provides a roadmap for future work.

## 1.2 Overview

The attraction to using the group III-Nitrides is because the semiconductors have wide direct bandgaps. 6.2 eV for AlN, 3.4 eV for GaN and 0.69 eV to 1.89 eV for InN. [1] As well each of the three can be combined in a variety of concentrations for ternary alloys. Because of this alloying, the optical absorption edge of the ternary alloys can be tuned to any desired optical absorption edge along the lines. This relationship can be seen in Figure 1 including bowing compensation.

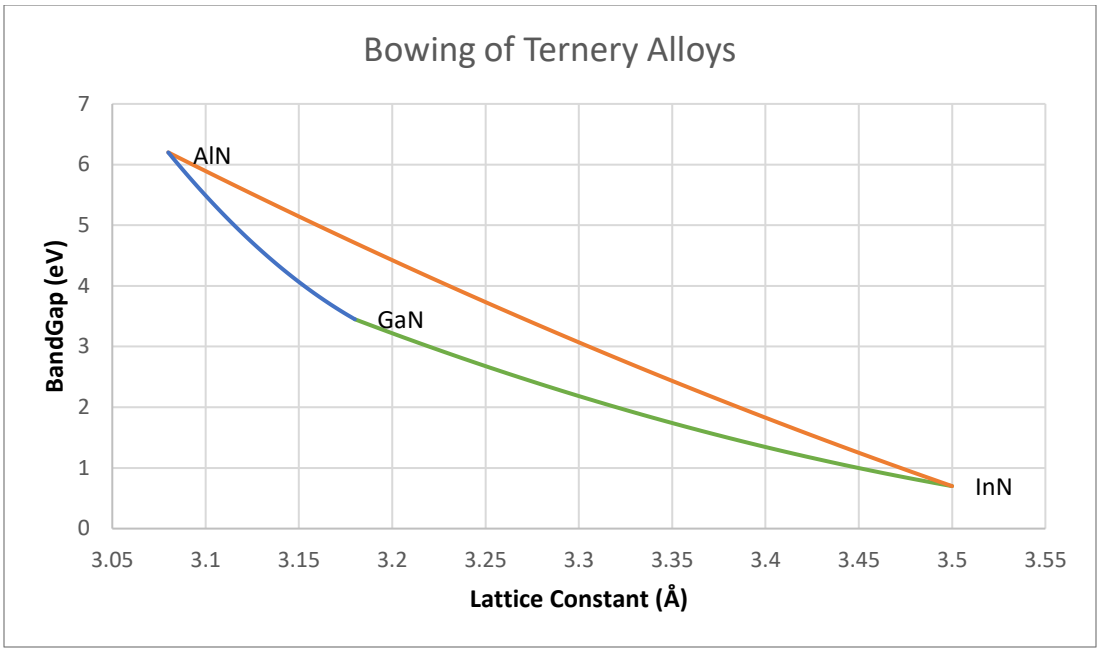


*Figure 1 Bowing of the Ternary Alloys of the Group III-Nitrides*

The bowing compensation is a parameter from an extension of Vegard's Law, which is a linear interpolation assuming both parts are the same crystal structure and the component elements are pure. [2] The extension comes from the addition of a bowing parameter C. This bowing parameter is to compensate for the curvature of the optical absorption edge.

$$E(A_{1-x}B_x) = xE_g(A) + (1-x)E_g(B) - x(1-x)C \quad (1)$$

Because of the above relationship and the wide range of available direct band gaps the III-V Nitrides are very attractive for devices. The earliest being the blue LED, but LEDs are not the only things that could possibly be made. The materials are invaluable for photovoltaics, and optoelectronic sensors. As well as, short wavelength laser diodes [3] and HEMTs [4]. HEMTs are of special interest due to the specific crystal properties of the III-V Nitrides.

The crystals can exist in one of three states. The most stable being wurtzite, and cubic zincblende. The rock salt phase can exist but is only formed under high pressures [5]. The wurtzite form of the crystal exhibits a spontaneous polarization along the c-axis which is shown in Figure 2.

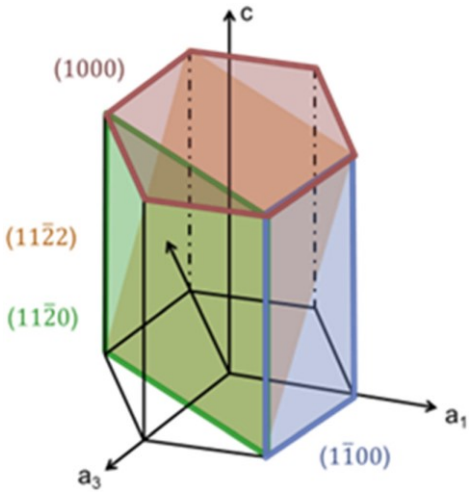


*Figure 2 Basic wurtzite crystal showing axis and common planes [6]*

Wurtzite crystals have the highest symmetry compatible with spontaneous polarization, Table 1 summarizes the basic properties of the group III-nitrides including the lattice parameters $a_0$ and $c_0$ along with the internal bond length between the nitrogen atom and metal atom, u. From the table GaN has the lowest spontaneous polarization and the closest ideal $\frac{c_0}{a_0}$. The ideal ratio being 1.633 (or $\frac{2\sqrt{6}}{3}$), this corresponds to an ideal $c_0 = \sqrt{\frac{8}{3}} * a_0$ along with an ideal $u = \frac{3}{8}$. The increasing non-ideality affects the spontaneous polarization, as $u$ gets larger and $\frac{c_0}{a_0}$ gets shorter $P_{sp}$ increases.

*Table 1 Basic properties of the III-V Nitrides*

| Material | GaN | InN | AlN |
|---|---|---|---|
| a0 (Å) | 3.189 | 3.540 | 3.112 |
| c0 (Å) | 5.185 | 5.705 | 4.982 |
| c0/a0 | 1.627 | 1.612 | 1.601 |
| u | 0.376 | 0.377 | 0.380 |
| Psp (C/m2) [7] | -0.029 | -0.032 | -0.081 |
| e33 (C/m2) [7] | 0.73 | 0.97 | 1.46 |

This spontaneous polarization gives way to the development of a 2DEG which will be spoken about further in Chapter 2.

In addition to the above electrical properties the materials exhibit robust physical properties. GaN and AlN have very high melting points (>1700°C and 3273°C respectively) along with a high thermal conductivity, 2.3 W/cm $K^{-1}$ for GaN and 3.2 W/cm $K^{-1}$ for AlN [1] which is much greater than silicon (1.3 W/cm $K^{-1}$) [8]. These physical properties along with the electrical properties make the III-N ideal for harsh environments such as space.

Despite these obvious advantages, the III-Nitrides have proven difficult to grow in bulk. Because of this, heteroepitaxy must be used. This presents a problem as there is a lattice mismatch between the III-N and the substrates needed for growth. The historical substrate has been sapphire, however there is a large mismatch between the layer and the sapphire substrate (17%). Research is moving into other substrates, such as SiC which has a lattice mismatch of only 3.4% (for GaN) and has compatible physical properties as the group III-Nitrides summarizes in Table 2.

*Table 2 Summary of the properties of SiC compared to GaN*

| Material | 6H-SiC | GaN |
|---|---|---|
| Bandgap (eV) | 3.0 | 3.4 |
| Thermal Conductivity (W/cm-K) | 3-5 | 1.3 |
| Electron mobility ($cm^2V^{-1}s^{-1}$) | 400 | 900 |
| $a_0$ (Å) | 3.073 | 3.186 |
| Dielectric Constant | 9.7 | 9.5 |

## 1.3 Motivation

The purpose of this work is to develop the necessary growth techniques needed to produce high quality layers of each of the III-N layer on a commercially purchased SiC template. Once each material has been successfully grown growth of the ternary alloys can begin to the eventually development of a device. In addition to the above growth of high quality layers, theoretical calculations using the linear combination of atomic orbitals for the analysis of impurity centers within the III-N layers, specifically carbon contamination within the InN cell.

# Chapter 2 Materials of Interest

## 2.1 Crystal Structures

This chapter covers each material of interest in greater detail. First there will be a small summary of the crystal structures that can be formed from each material and the differences between them. Next the physical and electrical properties of GaN will be covered. The same will be done with AlN and InN. For the alloys, they are just extensions of the individual materials and depending on their composition ($A_xB_{1-x}N$) will have their electrical properties changed. The physical properties however, will remain the same.

As stated in the Chapter 1 the group III nitrides can exist in one of three phases: the thermodynamically stable wurtzite, zincblende and in rock salt. The rock salt phase can only exist under high pressures: 22.9 GPa for AlN [9], 52.2 GPa for GaN [10] and 12.1 GPa for InN [11], the reason for this is that the reduction in the lattice dimensions causes interionic Coulomb interactions which favor the iconicity over the covalent nature. The rock salt phase cannot be formed by any epaxial means but is instead formed in a diamond anvil cell from the wurtzite state.

### 2.1.1 Cubic/Zincblende

The cubic crystal structure is most commonly seen in the traditional semiconductors, like Si and Ge, but are also phases of the group III Nitrides as well. These structures have three main varieties, primitive cubic (Pc), body centered cubic (bcc) and face centered cubic (fcc), these varieties can be seen in Figure 3.

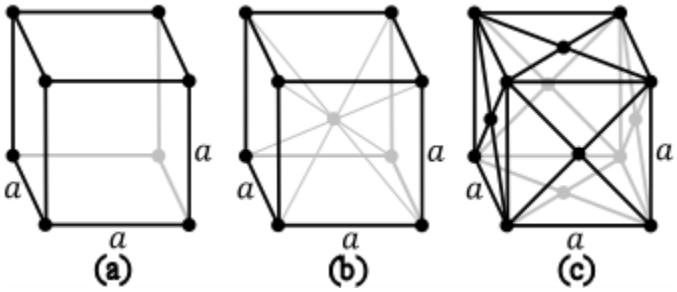


*Figure 3 The three varieties of cubic systems (a) primitive, (b) body centered (c) face centered*

The benefit of a cubic system is full 3D symmetry, in effect, no matter which direction force is applied there is no net change to the charge distribution. Each of the III-N can be present in a cubic system, however, these crystals are metastable and will be talked about in their respective sections.

The Zincblende cubic, of which the III-N belong, is a type of face centered cubic (c in Figure 3) is named after the mineral zincblende (or sphalerite, one form of ZnS). Each atom's nearest

neighbor consists of an atom of the opposite type. Other compounds that show the zincblende structure are diamonds, other III-V compounds like GaAs or AlAs, and lead(II) nitrate.

### 2.1.2 Wurtzite

Most of the time the group, III-nitrides will form into the wurtzite crystal structure. This is the most thermodynamically stable structure for the III-nitrides. Wurtzite, unlike zincblende, does not have uniform symmetry and any stresses or strains upon the structure will cause a spontaneous polarization. Wurtzite can be described as two interpenetrating hexagonal close packed structure with a translation of 5/8 of the lattice constant $c_0$. Figure 4 shows the unit cell of a wurtzite crystal along with some of the physical dimensions of the III-N.

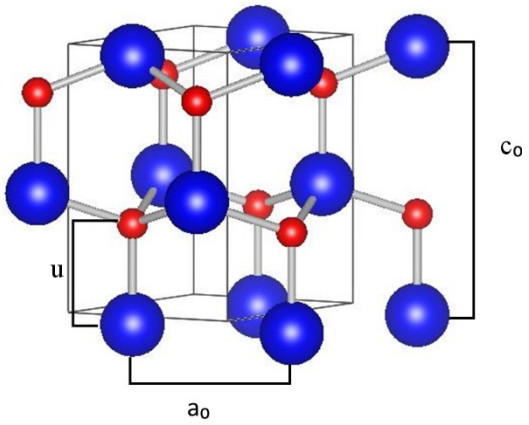


| Material | GaN | InN | AlN |
|---|---|---|---|
| $a_0$ (Å) | 3.189 | 3.540 | 3.112 |
| $c_0$ (Å) | 5.185 | 5.705 | 4.982 |
| $c_0/a_0$ | 1.627 | 1.612 | 1.601 |
| u | 0.376 | 0.377 | 0.380 |

*Figure 4 Unit cell of wurtzite crystal showing the tetrahedral structure along with the physical dimensions of the III-nitrides.*

Stacking in a wurtzite crystal is done in a hexagonal close packed system or ABABAB. This means that every other layer will be the same. This type of stacking can be seen in Figure 5. It is important to note that the orientation of the metal to nitrogen atoms as it effects the polarization of the crystal. When the metal is facing the top of the c-plane the crystal (referred to as Ga-Polarity) the crystal is in the [0001] orientation. When the nitrogen atom is on top of the c-plane (referred to as N-polarity) the crystal is in $[000\bar{1}]$ orientation. [12]

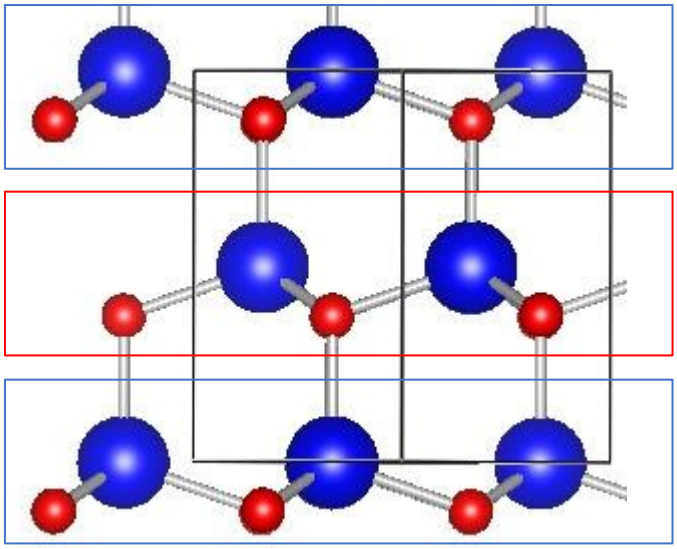

*Figure 5 Stacking in a wurtzite crystal in the ABABAB format. The blue outline is A and the red outline is B*

## 2.2 Gallium Nitride

Gallium Nitride is the most well-known of the group 3 nitrides. It is used in a variety of electronic devices in both pure form and in a ternary alloy, for example, a GaN/AlGaN HEMT [13]. GaN is the basic material used in devices, as well most ohmic contacts are either n-doped or p-doped GaN.

### 2.2.1 Mechanical Properties

As stated above GaN can exist in one of three phases with the wurtzite being the most stable. Table 3 gives the mass density of GaN along with the other materials of interest. Table 4 is a comparison between the different Vickers hardness H and the fracture toughness $K_c$.

Table 5 and Table 6 compile the elastic constants of the III-N and the coefficients of thermal expansion respectively.

*Table 3 Mass density of the III-N and SiC. [14]*

| Material | GaN | AlN | InN | SiC | Si |
|---|---|---|---|---|---|
| Mass Density ($g/cm^{-3}$) | 6.1 | 3.23 | 6.81 | 3.21 | 2.33 |

*Table 4 Vickers's hardness H and the fracture toughness $K_c$ of the III-N with Si as a reference. [13]*

| Material | GaN | AlN | InN | SiC | Si |
|---|---|---|---|---|---|
| H (GPa) | 12 | 14 | 11.2 | 33 | 9 |
| $K_c$ ($MPa\sqrt{m}$) | 0.8 | 2.6 | — | 3.3 | 0.7 |

*Table 5 Elastic properties of the group 3 nitrides. [15]*

| Material | GaN | AlN | InN |
|---|---|---|---|
| $C_{11}$ (GPa) | 390 | 396 | 223 |
| $C_{33}$ (GPa) | 398 | 373 | 200 |
| $C_{44}$ (GPa) | 105 | 116 | 48 |
| $C_{12}$ (GPa) | 145 | 137 | 115 |
| $C_{13}$ (GPa) | 106 | 108 | 92 |

*Table 6 Thermal expansion coefficient (CTE) of the semiconductors at room temperature. [12]*

| Material | GaN | AlN | InN | SiC | Si |
|---|---|---|---|---|---|
| $a_a$ ($10^{-6}$ $K^{-1}$) | 3.1 | 2.9 | 3.6 | 3.2 | 2.6 |
| $a_c$ ($10^{-6}$ $K^{-1}$) | 2.8 | 3.4 | 2.6 | 3.2 | 2.6 |

All three of the group 3 nitrides have similar hardness while silicon carbide is very hard. From the elastic constants, the bulk modulus, $B$, (or compressibility$^{-1}$) for GaN can be determined.

$$B = \frac{[C_{33}\cdot(C_{11}+C_{12})-2(C_{13})^2]}{[C_{11}+C_{12}-4C_{13}+2C_{33}]} \quad (2)$$

$$B_{GaN} = 210\ GPa \quad (3)$$

This number is how uncompressible the material is and the larger the number the less compressible the material is. This value is important only in the bulk materials and not as useful when growing epitaxially.

The coefficient of thermal expansion is how much the materials change in size due to heat. This value is important as the materials are grown at a high heat and cool down to room temperature, causing stress. If the mismatch percentage between the grown layer and the substrate are too large, the crystals may form large defects, which would cause problems with the electrical properties in a device fabricated from those layers.

### 2.2.2 Electrical Properties

The electrical properties of GaN are well understood. Table 7 shows a compilation of the dielectric constants of the materials along with Si as a reference as well as the band gap energies and electron and hole mobilities. All the III-N have type-I transition energy barriers (or direct bandgaps) which, in conventional heterostructures, the band alignments are symmetrical. In highly polar semiconductors like the III-N however this is not always the case, due to strains caused by the substrate, and the resulting strain on the top grown thin layer polarization charge develops. This polarization charge density is summarized in Table 8. Table 9 shows the thermal conductivity and thermal mismatch of each material along with the lattice mismatch. The thermal mismatch is important since the crystals are grown at high temperatures and will cool at different rates. The larger the mismatch the higher the probability of the crystals cracking forming defects.

*Table 7 Electrical properties of the III-N and other related materials. [12], [16]*

| Material | GaN | AlN | InN | SiC | Si |
|---|---|---|---|---|---|
| Dielectric Constant | 9.5 | 8.5 | 15.3 | 6.52 | 11.9 |
| Bandgap (eV) | 3.4 | 6.2 | 0.7-1.8 | 3.3 | 1.12 |
| Electron Mobility ($cm^2/V \cdot s$) | 1000 | 300 | 3200 | 980 | 1500 |
| Hole Mobility ($cm^2/V \cdot s$) | 200 | 14 | 220 | 200 | 400 |

*Table 8 Spontaneous and piezoelectric polarization of the III-Nitrides. [7]*

| Material | GaN | AlN | InN |
|---|---|---|---|
| $P_{sp}$ ($C/m^2$) | -0.029 | -0.081 | -0.032 |
| $e_{33}$ ($C/m^2$) | 0.73 | 1.46 | 0.97 |

The polarization charges arise from the crystal structure itself. As GaN has the closest c/a to the ideal value, the polarization charge is quite weak compared to the other two. As stated earlier the increasing non-ideality of the crystals affects the polarization, as u gets larger and c/a gets shorter the spontaneous polarization increases.

*Table 9 Coefficient of thermal expansion and lattice constant of the materials of interest along with the mismatch between the layer and the substrate. [12], [17]*

| Material | GaN | AlN | InN | SiC |
|---|---|---|---|---|
| $\alpha_a$ ($K^{-1}$) | 3.1 | 2.9 | 3.6 | 3.2 |
| Thermal Mismatch (%) | -3.13 | -9.375 | 12.5 | — |
| $a_0$ (Å) | 3.189 | 3.1106 | 3.501 | 3.081 |
| Lattice Mismatch (%) | 3.08 | 0.96 | 13.63 | — |

If the thermal mismatch is less than zero the film will undergo a compressive strain, while greater than zero will result in a tensile strain. For the lattice mismatch the same principle applies.

## 2.3 Aluminum Nitride

Second to GaN, AlN is the most important binary material. Mostly used alloyed to GaN to make $Al_xGa_{1-x}N$ in heterostructured devices. Since the band gap of AlN is so high, the material is characterized to be an insulator. Typically AlN is used as a nucleation or buffer layer between the substrate and the grown layer, especially on sapphire, and as an interlayer at the channel/barrier interface in devices [18].

### 2.3.1 Mechanical Properties

The basic properties of AlN have been summarized in the tables above. The mass density of AlN is much smaller than GaN or InN. The hardness and thermal expansion are roughly the same as GaN with AlN being lower. The elastic properties are given in Table 5 which gives a bulk

modulus of $B_{AlN} = 207\ GPa$. The CTE of AlN is the lowest of all the III-V nitrides, this makes AlN a potentially attractive substrate. In addition, the lattice mismatch between AlN and SiC is the lowest of the three semiconductors.

### 2.3.2 Electrical Properties

With its large bandgap, AlN can be alloyed GaN to produce a structure with a bandgap between AlN and GaN. An even larger range can be accomplished with InN in the form of $In_xAl_{1-x}N$. The electron and hole mobility of AlN is weaker than the other two.

## 2.4 Indium Nitride

InN is the least understood the of the III-N, due to its relatively difficult to grown bulk crystals. Typically , like AlN, InN is used in its ally states of $In_xAl_{1-x}N/GaN$ [4] and $In_xAl_{1-x}N/Al_xGa_{1-x}N$ [19]. The indium content is usually low to achieve a lattice match with GaN. In recent years InN growth using MBE [20] and plasma enhanced ALD [21] has been achieved.

### 2.4.1 Mechanical Properties

Due to the lack of bulk materials of InN there is some uncertainty with the above mechanical properties. The CTE in Table 6 are from growths of InN on sapphire. The thermal properties are based off extrapolations, much is the same with some of the electrical properties. InN also suffers from disassociation at higher temperatures during growth necessitating a low growth temperature which limits the use of typical MOCVD reactors. From the elastic properties, a bulk modulus of $B_{InN} = 137\ GPa$ is found.

### 2.3.2 Electrical Properties

Because of the above motioned lack of bulk materials and the need for growth of InN on sapphire, some of the electrical properties such as the band gap have been difficult to pinpoint

which is why there is a range of values from 0.67 [22] to 1.89 [23]. Aside of the issue of the bandgap, InN has the highest mobility of the three nitride based semiconductors which, when alloyed, can have a great impact on the operation of devices.

## 2.5 Silicon Carbide

Silicon carbide has a benefit of being able to withstand high temperatures and high power, making it an ideal replacement for traditional silicon substrates for those type of applications. SiC based MOSFETS and diode rectifiers would be able to operate at higher voltages and temperature ranges, have superior switching, and have 20 times smaller die sizes than the corresponding rated silicon devices. [24]

### 2.4.1 Mechanical and Electrical Properties

Silicon carbide exists in many different crystal structures called polytypes. The most common polytypes being developed are 3 cubic silicon carbide (3C-SiC), 4 hexagonal silicon carbide (4H-SiC) and 6 hexagonal silicon carbide (6H-SiC). The different polytypes of SiC are composed of different stacking sequences of Si-C bilayers as shown in Figure 6. The polytype of interest for this thesis is 6H-SiC.

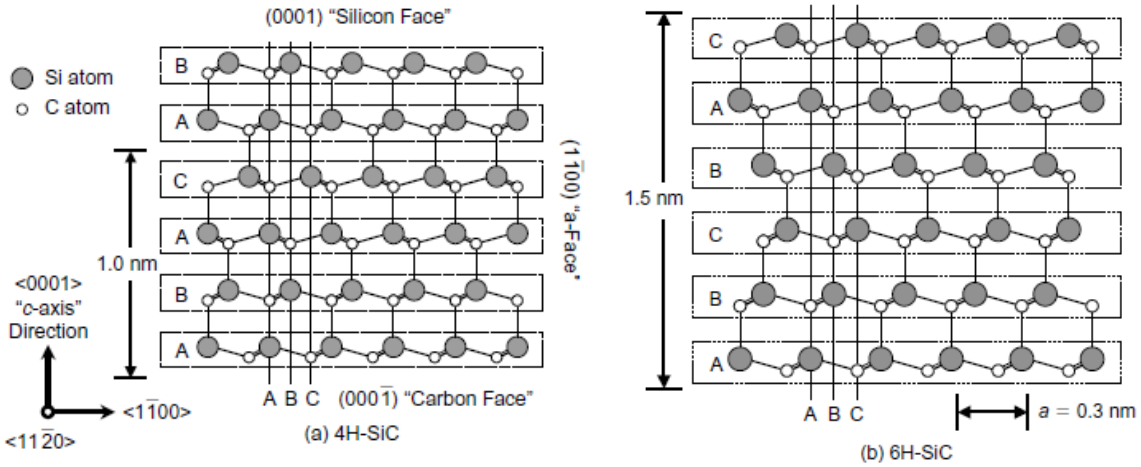


*Figure 6 Cross section of (a) 4H-SiC and (b) 6H-SiC atomic crystal structure showing direction and surface faces [25]*

Owing to the differing arrangements of SiC, each polytype displays different electrical properties. The electrical characteristics in Table 7 are for 6H-SiC. These properties, along with the similar lattice structure and CTE make SiC an ideal substrate for the growth of III-N due to the very low mismatch [26]–[28]. However, there remain a number of issues with SiC these issues are: 1) micropipe defects, 2) surface polishing to reduce roughness, 3) availability of standard size wafers and 4)dislocations [29]. Micropipes are screw defects with larger Burger's vectors stretching though the complete crystal during bulk growth. Limiting the amount of micropipes and mechanical polishing of the substrate to lower the RMS roughness are needed to address the stated issues.

The substrates for this thesis were commercially purchased SiC on Si with a layer of GaN deposited on to the SiC.

# Chapter 3 Characterization Techniques

## 3.1 X-Ray Diffraction

### 3.1.1 Theory

X-ray diffraction (XRD) is a non-destructive measurement technique for characterizing the crystal structure of solid samples. It provides information on the lattice parameters (for strain and composition measurements), misorientation, wafer bowing, residual stress and non-uniformities.

Diffraction of a crystal involves probing a sample with x-ray radiation that has a close wavelength ($\lambda$) to the crystal lattice. X-rays are generated by bombarding a metal (typically copper) with electrons in an evacuated tube, and monochromatic x-rays are selected. These x-rays are scattered by the electron cloud of each atom in the crystal. Constructive interference occurs

between the electrons when the path difference is equal to $2d \cdot \sin\theta$. This is the basis for Bragg's law which can be seen in Figure 7.

$$n\lambda = 2d \cdot sin\,\theta \qquad (4)$$

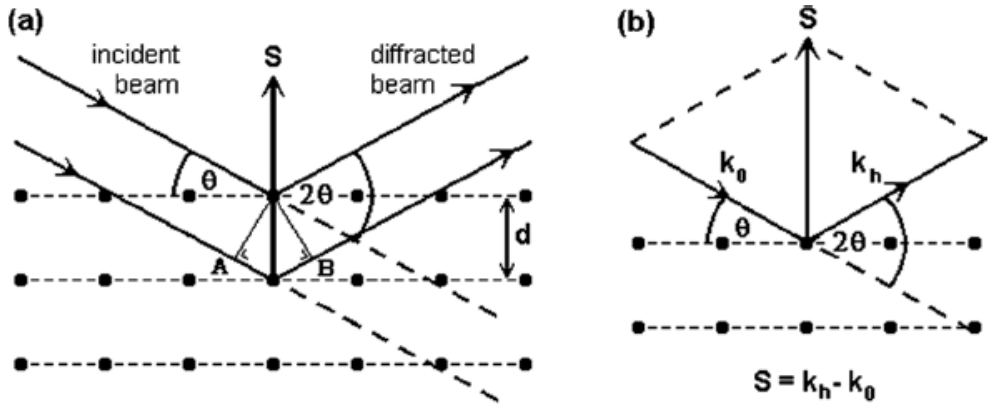


*Figure 7 (a) Bragg's condition for x-ray diffraction and (b) relationship between incident ($k_0$), diffracted ($k_h$) and the scattering vector S with respect to the crystal. [30]*

Experimentally, the angle 2θ is measured. The crystal acts as a 3D grating, so that as the detector and the source are moved, a 3D array of diffraction maxima can be explored. For hexagonal crystals, a four index (*hkil*) notation is used. The additional redundant index, *i* equal to –(*h*+*k*), helps to show the equivalency of planes. A summary of notation convention is given in Table 10.

*Table 10 Summary of notation convention between the three and four index notation.*

| Three Index Notation | Four Index Notation | Meaning |
|---|---|---|
| 102 | 10-12 | Reflection |
| (102) | (10-12) | Plane |
| {102} | {10-12} | Family of Planes |
| [102] | [10-12] | Direction |
| <102> | <10-12> | Family of Directions |

Diffraction in the crystal can be visualized by the incident and diffracted beam vectors ($k_0$ and $k_h$ respectively) making an appropriate angle with respect to the crystal, then the scattering vector, S, will end at a reciprocal lattice point. S in this case is the 'probe' used to investigate the lattice and its length is changed by changing 2θ. When S is at the right angle a diffraction peak can be measured, rarely however, is the peak sharp. Defects in the crystal, limitations of the measuring resolution and the macroscopic size and shape of the sample (such as wafer bending) serve to broaden the diffraction peak. As such the full width at half maximum (FWHM) is used to measure the quality of the crystal. The smaller the FWHM the better the crystal quality. [30]

### 3.1.2 Measurement Technique

Measurement of the XRD is done using the Philips PanAlytical X'Pert Pro MPD in θ-2θ mode. In this mode the emitter and detector are kept at the same angle relative normal to the sample, and varied though the angles (θ) at a specified degree per step. The k-$\alpha_1$ peak was used with an accelerating voltage of 45KV and a tube current of 40mA. k-$\alpha_2$ and k-β peak are filtered out by the software and the k-$\alpha_1$ gives the highest peaks.

## 3.2 Scanning Electron Microscope

### 3.2.1 Theory

The scanning electron microscope is a surface measuring tool which utilizes a focused beam of electrons to scan a sample of interest. The SEM can give images to a 1nm resolution with very little sample preparation compared to other techniques such as transmission electron microscopy (which requires ion milling to get an atomically flat sample). The electrons are generated using a filament which generates thermionic emissions under a vacuum of $10^{-7}$ Torr to increase the mean free path to practical lengths. The electrons are accelerated under a high voltage and focused through a series of condenser lenses. The final lens deflects the beam in the x and y direction to

produce a raster over the sample area. When the electrons hit the sample the electrons lose energy, by absorption or by scattering within the bloom called the interaction volume, which is seen in Figure 9. The size of which can vary from 10's of nm to the µm range depending on the power of the electron beam and the density and atomic number of the element being scanned. A variety of detectors are used to identify the backscattering electrons, secondary electrons, Auger electrons and characteristic x-rays.

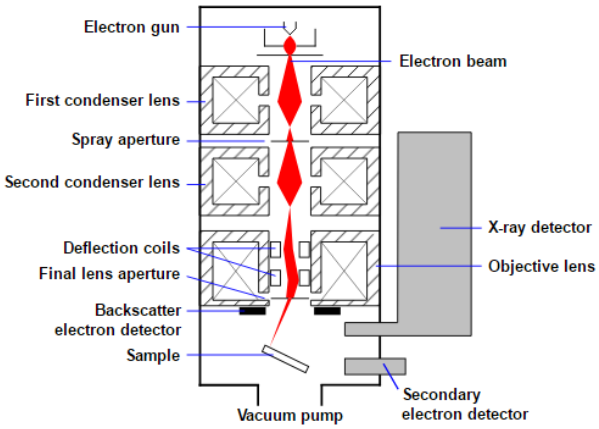


*Figure 8 Schematic of a typical SEM beam and electron gun. [31]*

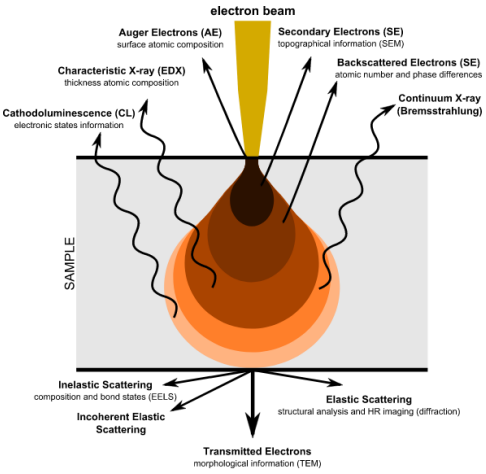


*Figure 9 Interaction bloom in a sample caused by the interacting electrons. [32]*

### 3.2.2 Measurement Technique

The sample is placed into the SEM under a vacuum of $10^{-5}$ Torr. Measurement is done using a Hitachi SU-70 located in the university. Samples can be loaded flat for surface measurements or in a holder on the side for cross-sectional views. Conductive carbon tape or paste is used to allow for a path to ground for the electrons. Copper tape or carbon sputtering can also be used as an alternative to the carbon paste. The addition of the carbon/copper increases the quality of the SEM image.

## 3.3 Energy-dispersive X-ray Spectroscopy

### 3.3.1 Theory

EDX is used for element determination of samples. The sample is hit with a high energy x-ray and excites one of the inner electrons ejecting it from the shell leaving an electron hole. An electron from an outer higher energy shell moves to fill the hole. The difference in energy between the higher energy and lower energy shell is then measured. As the energy of the x-ray is characteristic to the energy difference between the two shells and of the atomic number of the emitting element, identification can be accomplished. Since EDX is done within an SEM scan the measurement technique is like SEM.

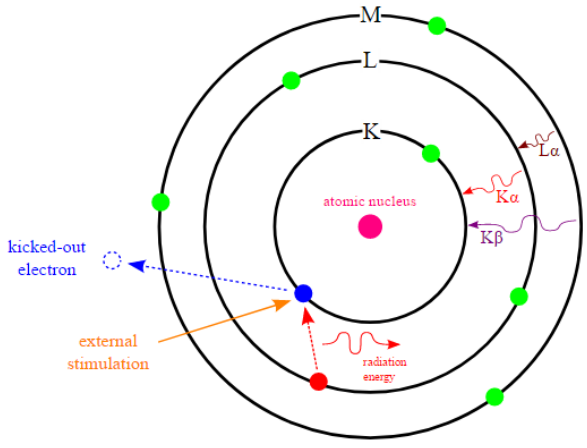


*Figure 10 Schematic on how an electron is removed from the K-Shell [33]*

## 3.4 Atomic Force Microscope

### 3.4.1 Theory

AFM is a non-destructive measuring technique used to determine the surface characteristics of a sample down to the atomic level with very little sample preparation. A fine tip is position over evenly spaced points in a desired scan area close to the sample. At each point the deflection on the cantilever arm is measured using a laser and a photodiode. Depending on the operating mode, different data/points are used to interpolate and map a false colour plot of the sample surface. Typically, in literature the RMS roughness is reported as a metric of the sample smoothness.

Cantilevers are often fabricated out of silicon using standard photolithography technology. This allows for high precision over the geometry and the ability to engineer tips with thin film coatings for a specific stiffness or other electrical properties. Positional control of the cantilever utilizes piezoelectric transducers for precise control of the tip along with stepper motors for macro movements of the scan head (approaching and withdrawing from the sample).

AFM has three general types of operating modes: contact, non-contact and tapping mode. In contact mode, the tip is brought close to the sample and static deflection of the cantilever is measured. The z-axis controller adjusts the distance to maintain a constant distance to the sample. In effect the tip is “dragged” across the sample. Because of this the cantilever needs to have a low stiffness to account for large variations in a rough sample. This type of scan is the slowest and most prone to noise. In addition, contact mode can damage fragile or soft samples such as oxides. The tips used are expensive and prone to breakage on very rough samples which is a prohibitive problem.

In opposition to contact mode is non-contact mode. In this mode, the cantilever is brought close (within a few nanometers) to the sample and oscillated at its resonant frequency. The tip is

loaded due to the Van der Waals force, or any other long-distance force which shifts the resonant frequency of the cantilever, which is monitored by the laser and photodiode. The z-axis controller is then used to adjust the distance of the probe to shift the resonance back to the original value. The controller response is used to determine the sample's topography. The main advantage of this technique is no contact is made with the sample surface and thus no damage is done, sparing fragile surfaces and increasing tip life. The main disadvantage is the tip can receive false readings due to surface contamination such as water from ambient humidity. When using this technique, the controller is given a percentage of vibrational amplitude to consider as the sample surface. The smaller the value the closer the tip. To extend tip life, the value should be as large as possible, however if the value is too large then the tip will not be close enough to the sample to get accurate readings.

Finally, in tapping mode, which is in between contact and non-contact. The tip is oscillated at the resonance frequency but brought close enough to the sample to experience contact forces from the sample surface. This technique has the benefits of non-contact mode (longer tip life and decreased wear on the sample) and from contact mode (protection from false readings caused by liquid contaminants).

### 3.4.2 Measurement Technique

AFM measurements are preformed using an AFM Nanosurf Easyscan 2 atomic force microscope. The probes used are ACL-A which contains a thin coating of aluminum on the top, a length of 225µm, width of 40µm, tip radius of <10nm, height of 14-16µm and a stiffness of 36-90 N/m. The typical scan area is 5µm x 5µm but can be varied to a max scan size of 8.89µm x 8.89µm and a minimum on the pm scale (typically the smallest scan is 1µm x 1µm as anything

smaller lack fine details). The scan area has 512 to 1024 points per line scanned at 1 to 2 seconds per line.

## 3.5 Raman Spectroscopy

### 3.5.1 Theory

Raman spectroscopy is a measurement technique which relies on inelastic scattering of photons from a laser source to identify vibrational, rotational and other low-frequency changes in molecules. When a laser is shined on a sample one of three possible re-emission effects happens. Elastic or Rayleigh scattering in which the photons are re-emitted at the same frequency of the laser. These emissions are filtered out. The second possibility is that the photon excites a molecular vibration within in the sample loses energy and is re-emitted at a lower frequency. Finally, the third possibility is that the photon is absorbed by a molecule which is already in an excited state from a previous event. In this possibility the photon re-emits from the molecule at a higher frequency. This shift in frequency of the laser is characteristic to the molecular bonds in the sample and after filtering the central frequency of the laser, information about the specific bond in the sample can be detected. This information helps to determine the chemical make-up of the samples.

Because of the mode of detection for the Raman system with the laser beam incident to the surface only the $E_2$ and the $A_1$(LO) modes are allowed. This give two distinct peaks in the Raman plot, this can be seen in Figure 11

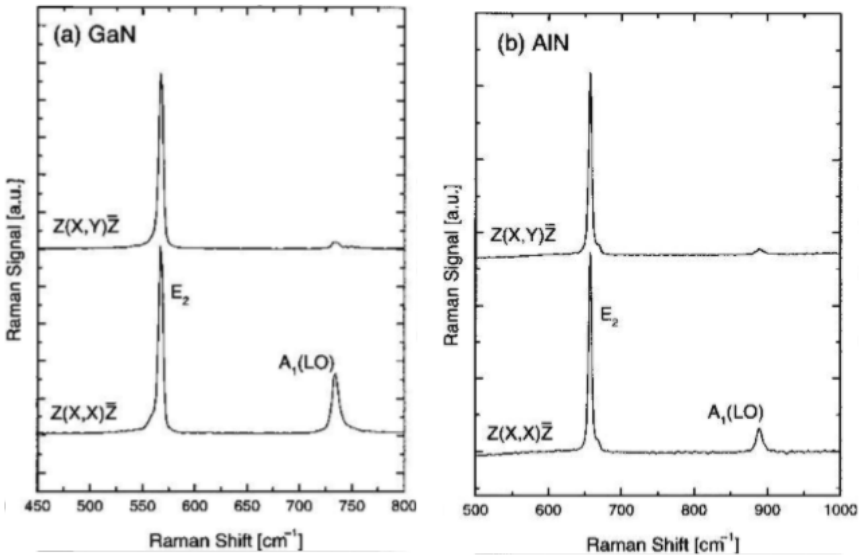


*Figure 11 Raman spectra for (a) GaN and (b) AlN at room temperature. [34]*

### 3.5.2 Measurement Technique

Raman measurements are carried out using a custom Raman set-up in Lakehead university. The laser is a 512nm green laser and the detector is a 250TS. The laser is shined on the sample though a Nikon e400 microscope to allow for spot selection, and the reflection from the laser is sent to the detector and the Raman shift is detected.

## 3.6 Hall Effect

### 3.6.1 Theory

If an electric current is passed through a conductor in a magnetic field, the magnetic field exerts a transverse force on the moving charge carriers which tends to push them to one side of the conductor. The buildup of charges at the side will balance out the magnetic field producing a measurable voltage between the two sides of the conductor. This is described as the Hall effect after E. H. Hall who discovered it in 1879.

The hall effect, at its heart, is an extension of the Lorentz force, the equation is given as

$$F = q(\vec{E} + \vec{v}\, x\, \vec{B}) \quad (5)$$

which shows the force from a charge q moving with velocity v though a magnetic field B. When current moves though conducting material with a known magnetic field normal to the material. The current will be deflected towards or away depending on the charger of the carriers, (negative for electrons and positive for holes). This charge is detected and reported.

The method used for calculating the hall coefficient is the Van der Pauw method. In this method four contacts are made at each corner, which can be seen in Figure 12 and a current is passed between 1 and 3 and the voltage is measured across 2 and 4, then the current is reversed running from 3 to 1. After that, the measurement regime is switched with current running through 2 and 4 with the measurement being taken at 1 and 3 (and again the current is also swapped). The magnetic field is supplied by a permanent tesla magnet. The magnet is initially inserted with one polarity when the measurement is taken then switched for the measurement to be taken again.

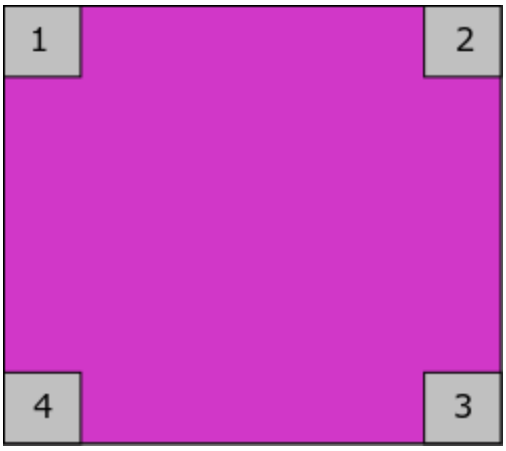


*Figure 12 Contact layout for the Hall effect*

Calculation of the hall voltage is found first then then the hall coefficient can be found. The hall voltage is found first by subtracting the positive magnetic field voltage by the negative magnetic field voltage ($V_{13} = V_{13P} - V_{13N}$ for example) this is done for all 8 voltages.

$$V_{13} = V_{13P} - V_{13N} \quad (6)$$

$$V_{24} = V_{24P} - V_{24N} \quad (7)$$

$$V_{31} = V_{31P} - V_{31N} \quad (8)$$

$$V_{42} = V_{42P} - V_{42N} \quad (9)$$

From the calculations done in (6)-(9) an average is taken

$$V_H = \frac{V_{13}+V_{24}+V_{31}+V_{42}}{8} \quad (10)$$

Using (10) the Hall coefficient can be found

$$R_H = \frac{V_H t}{BI} \quad (11)$$

Where t is the thickness of the film, B is the magnetic field and I is the current.

### 3.6.2 Measurement Technique

Measurement of the Hall coefficient is done using a Ecopia HMS-3000 Hall Effect Measurement System. The permanent magnet is a 1 Tesla magnet, and the current is typically 1mA. The system can also take an IV curve to verify the conductivity of the film being measured. In addition to the hall coefficient the system can also find resistivity, sheet concentration and conductivity.

# Chapter 4 Growth Process

Growth of the III-V Nitrides can be accomplished using a variety of techniques and regimes including Atomic Layer Deposition (ALD), Molecular Beam Epitaxy (MBE), Hydride Vapour Phase Epitaxy (HVPE) and Metal-Organic Chemical Vapour Deposition (MOCVD). A summary of the different techniques can be seen in Table 11. As the reactor at Lakehead University is a type of MOCVD reactor, focus will be given to that growth technique.

*Table 11 Different types of growth techniques and their comparisons.*

| Technique | Growth Pressure Range (Torr) | Growth Temperature Rage (°C) | Growth Rate | Nitrogen Source |
|---|---|---|---|---|
| **ALD** | 1 [35] | 150-400[35] | 2 Å/cycle [35] | Plasma or $NH_3$ |
| **MBE** | $10^{-5}$ [1] | 550-800[1] | 1 µm/h [1] | Plasma or $NH_3$ |
| **HVPE** | 760[36] | 1050-1200 [2] | 1 to 100 µm/h [2] | $N_2H_3$ |
| **MOCVD** | 10-760 [37] | 200-1100[1] | 1.8 to 60 µ/h[1] | Varied[1] |

## 4.1 MOCVD Growth Theory

MOCVD growths are complex and involve a series of gas-phase and surface reactions. Typically, MOCVD is performed at moderate pressures (as compared to MBE) and a wide range of temperatures (higher than ALD). The reaction can be visualized in Figure 13.

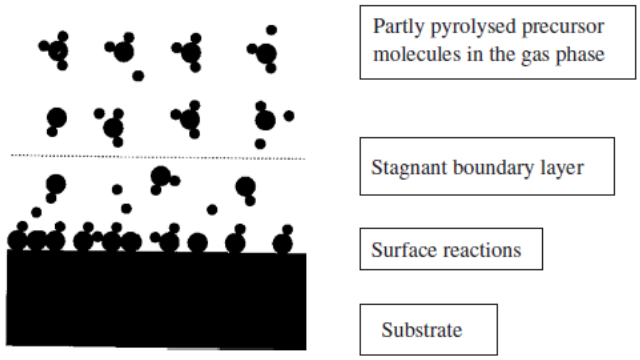


*Figure 13 Simple schematic representation of the MOCVD process. [37]*

A feature of the process is the stagnate boundary layer of hot gas right above the substrate. At these pressures pyrolysis reactions occur which play a significant role in the deposition process. The basic steps of the MOCVD reaction can be summarized as follows:

1. Evaporation and transport of the precursors into the reactor.
2. Gas phase reactions of the precursors in the reaction zone to produce reactive intermediaries and by-products.

3. Mass transport to the substrate surface.
4. Adsorption of the reactants on the substrate surface.
5. Surface diffusion to growth sites, nucleation and surface chemical reactions leading to film formation.
6. Desorption and mass transport of remaining fragments of decomposition away from the reaction zone.

In traditional MOCVD, the growth rate is determined by several parameters, with the primary ones being the temperature of the substrate, operating pressure of the reactor and composition of the gas-phase. As the temperature increases growth rate becomes nearly independent of the temperature and instead relies on the on the mass transport of the reagents. The operating pressure determines the importance of the gas-phase reactions. At around 760 Torr (or 1 atm) down to moderate pressures (10 Torr) the gas-phase is important, and a significant boundary layer is present. The mass transport and kinetics play an important role in deposition. As the pressure drops (<1 Torr) the gas-phase reactions become less important and the surface reactions control the growth rate. [37]

### 4.1.1 Precursors

There are two types of precursors Group III precursors and Group V precursors. However, no matter what type of precursor, the characteristics of the them must satisfy most of the following list:

- Adequate volatility to achieve acceptable growth rates at moderate evaporation pressures.
- Stability so that decomposition does not occur during evaporation
- A large temperature ‘window’ between evaporation and decomposition for film deposition
- High chemical purity

- Clean decomposition without the incorporation of residuals
- Long shelf-life with indefinite stability under ambient conditions. (unaffected by air)
- Readily manufactured in a high yield at low cost
- Low-hazard risk

The metal organic compounds used for the group III precursors are molecules that contain large function groups (allyl, butyl, methyl, ethyl etc.) or ligands (carbonyls etc.) some examples include trimethylgallium (TMG), triethylgallium (TEG), and bis(cyclopentadienyl)magnesium ($Mg(C_5H_5)_2$).

The group V precursors can be again a variety depending on which element is used. If nitrogen is the desired element, historically, ammonia ($NH_3$) is used. However, because of temperature constraints (such as the fact that InN decomposes at temperatures above 550°C) other sources can be used. Sources such as hydrazine ($N_2H_4$) which decomposes at temperatures lower than ammonia [38], or $N_2$ plasma can be used (which will be discussed in 4.2 Plasma Enhanced MOCVD). Table 12 shows a summary of common precursors used with MOCVD reactors along with their vapour pressures, hazards and their physical state at room temperature.

*Table 12 Common precursors [37]*

| *Precursor* | *Acronym* | *Formula* | *Physical state* | *Main hazard* | *Vapor pressure data* | *Density ($g\,cm^{-3}$)* |
|---|---|---|---|---|---|---|
| **Group III** | | | | | | |
| Trimethylgallium | TMG | $(CH_3)_3Ga$ | Liquid | Pyrophoric | $Log_{10}P(mmHg) = 8.07–1703/T(K)$ | 1.151 |
| Triethylgallium | TEG | $(C_2H_5)_3Ga$ | Liquid | Pyrophoric | $Log_{10}P(mmHg) = 8.08–2162/T(K)$ | 1.06 |
| Trimethylaluminium | TMA | $(CH_3)_3Al$ | Liquid | Pyrophoric | $Log_{10}P(mmHg) = 8.22–2134/T(K)$ | 0.752 |
| Triethylaluminium | TEA | $(C_2H_5)_3Al$ | Liquid | Pyrophoric | 0.02 mmHg @20 °C; 0.14 mmHg@40 °C | 0.835 |
| Trimethylindium | TMI | $(CH_3)_3In$ | Solid | Pyrophoric | $Log_{10}P(mmHg) = 10.52–3014/T(K)$ | 1.568 |
| **Group V** | | | | | | |
| Arsine | | $AsH_3$ | Gas | Toxic | $Log_{10}P(mmHg) = 6.569–762.4/T(K)$; bp = –62.5 °C | 3.29 kg $m^{-3}$ at 15 °C |
| Phosphine | | $PH_3$ | Gas | Toxic | $Log_{10}P(mmHg) = 6.984–754.1/T(K)$; bp –87.7 °C | 1.45 kg $m^{-3}$ at 15 °C |
| Ammonia | | $NH_3$ | Gas | Toxic | bp –33.35 °C, mp –77.7 °C | 0.5967 g $L^{-1}$ |
| *tert*-Butylarsine | TBA | $(t\text{-}C_4H_9)AsH_2$ | Liquid | Toxic | $Log_{10}P(mmHg) = 7.5–1562.3/T(K)$ | 1.0 |
| *tert*-butylphosphine | TBP | $(t\text{-}C_4H_9)PH_2$ | Liquid | Toxic | $Log_{10}P(mmHg) = 7.586–1539/T(K)$ | 0.7 |
| Unsym-dimethylhydrazine | DMHz | $(CH_3)_2NNH_2$ | Liquid | Reactivity | $Log_{10}P(mmHg) = 8.19–1780/T(K)$ | 0.791 |
| Trimethylantimony | TMSb | $(CH_3)_3Sb$ | Liquid | Pyrophoric | $Log_{10}P(mmHg)=7.73–1709/T(K)$ | 1.528 |
| Triethylantimony | TESb | $(C_2H_5)_3Sb$ | Liquid | Pyrophoric | $Log_{10}P(mmHg)=7.90–2183/T(K)$ | 1.324 |
| Tris(dimethylamino)antimony | TDMSb | $[(CH_3)_2N]_3Sb$ | Liquid | Flammable | $Log_{10}P(mmHg) = 6.23–1734/T(K)$ | 1.3 |
| **Dopants** | | | | | | |
| Dimethylzinc | DMZ | $(CH_3)_2Zn$ | Liquid | Pyrophoric | $Log_{10}P(mmHg) = 7.80–1560/T(K)$ | 1.386 |
| Diethylzinc | DEZ | $(C_2H_5)_2Zn$ | Liquid | Pyrophoric | $Log_{10}P(mmHg) = 8.28–2109/T(K)$ | 1.20 |
| Bis(cyclopentadienyl) magnesium | BisMg | $Cp_2Mg$ | Solid | Pyrophoric | $Log_{10}P(mmHg) = 10.0–3372/T(K)$ | – |
| Carbon tetrachloride | | | Liquid | | $Log_{10}P(mmHg) = 8.05–1807/T(K)$ | 1.59 |
| Carbon tetrabromide | | $CBr_4$ | Solid | | $Log_{10}P(mmHg) = 7.78–2346/T(K)$ | 3.42 |
| Silane | | $SiH_4$ | Gas | Pyrophoric | $Log_{10}P(mmHg) = 7.06–680.4/T(K)$: bp –111 °C | 1.35 kg $m^{-3}$ at 15 °C |
| Diethyltelluride | DETe | $(C_2H_5)_2Te$ | Liquid | Flammable | $Log_{10}P(mmHg) = 7.99–2093T$(K | 1.599 |
| Bis(cyclopentadienyl)iron | | $Cp_2Fe$ | Solid | | $Log_{10}P(mmHg) = 10.27–3680/T(K)$ | – |

### 4.1.2 MOCVD Reactor Design

No matter the precursor, the design of a MOCVD reactor follows basically the same design and consists of three major components, the gas delivery system, the growth chamber and the exhaust system. Every reactor will have those three main components along with any other options that the designer put in (for example a RGA to analyze exiting gases). Figure 14 shows an example schematic of a MOCVD reactor with the components shown.

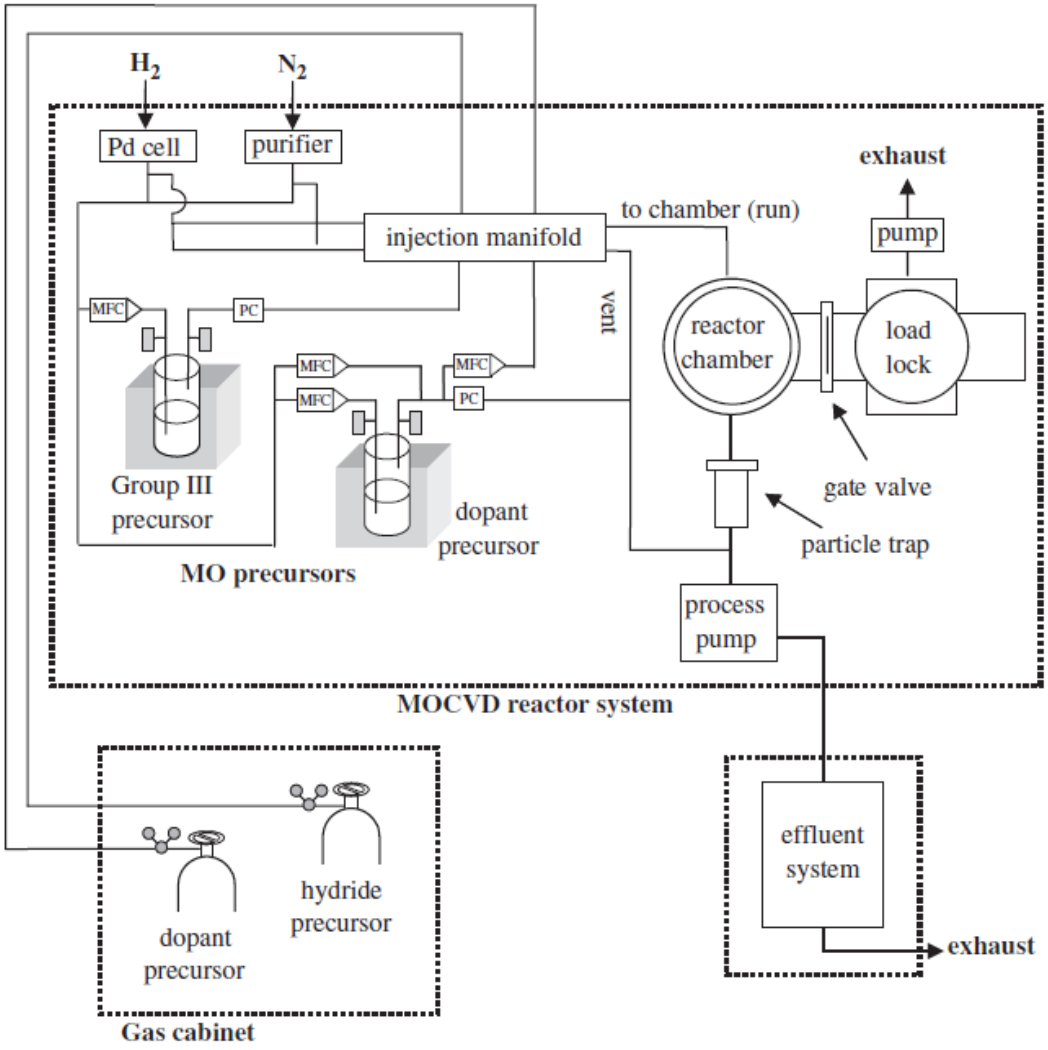


*Figure 14 Schematic diagram of a MOCVD reactor. [37]*

Each system accomplishes a specific task and must do so safety, seals between gas pipes are made using O-rings, gaskets, compression tube fittings (Swagelok) or welds. Welds are the safest but are inflexible and cannot be removed if relocation or disassembly is necessary and so are limited to areas that do not need to be moved. Because the precursors can react with other metals stainless steel is used as the material of choice for all tubes and reactor walls.

For the gas delivery system precursors at room temperature are in a liquid or sold phase and a carrier gas is 'bubbled' though them to carry the precursor vapour to the chamber. Every line is controlled by a valve and a mass flow controller which is routed through to a computer for accurate control. The valves can be pneumatically driven and/or a solenoid valve, these are part of the injection manifold.

The growth chamber is where the reaction takes place and thus contains all the necessary sensory equipment to maintain the proper atmosphere for growth. The chamber contains a heater, temperature probes, substrate rotation systems, pressure gauges, and a gas injection system (called a shower head). In addition, the growth chamber will have direct access to the exhaust system.

The exhaust system is used not only for removal of precursor byproduct but also to maintain the required background pressure needed for growth. These include turbo-molecular pumps, backing pumps, computer controlled variable valves and scrubbers. The scrubbers are necessary as some of the exiting precursors could be toxic to the atmosphere and can be made up of activated carbon, chemicals which react with the exiting gases to neutralize them or even thermal energy (which could produce a stable oxide).

## 4.2 Plasma Enhanced MOCVD (PEMOCVD)

Plasma is any gas that has a significant percentage of atoms or molecules are ionized. Plasma can be created by radio frequency (RF), electron cyclotron resonance (ECR)/microwave or direct

current (DC). The benefit of using a plasma is 1) the elimination of a precursor to a more pure gas and 2) lower growth temperatures. [39] Conventional PEMOCVD has several disadvantages with the main ones being:

- Plasma bombardment of the growing film can result in pinholes
- The process parameters (RF power, gas composition, gas pressure etc.) are interdependent and the individual influence of each is difficult to control
- Unpredictable results due to many reacting species caused by complex reactions

A workaround to the above stated problems is the use of remote plasma MOCVD (RPMOCVD). In this technique, the plasma is generated outside the area used for the substrate so that only some of the input reactants are excited by the glow discharge and transported to the reaction zone. Active species formed in the generation region and in the afterglow region are delivered to the substrate region, where they can react with the non-excited reactants or on the substrate surface to form a film.

## 4.3 Lakehead University Semiconductor Research Lab Reactor Growth

The reactor at Lakehead university is a modified version of a remote plasma MOCVD reactor. They system consist of three chambers each of which has its own vacuum system, a plasma source, a gas cabinet and a human machine interface (HMI).

The three chambers consist of a load lock, RGA chamber and the main reactor chamber that connects all other components. Each chamber's vacuum system is made up of a mechanical rotary vane pump (Leybold D16A for the RGA and load lock, and an Edwards E2M40 for the chamber) along with a turbo molecular pump to provide the necessary background pressure. The turbo pump on the main chamber is cooled via water and air as the pressure variations within the chamber would damage the pump if it was only air cooled.

Samples are loaded initially into the load lock on the transfer arm. The use of a load lock system is standard for high vacuum systems and allows for loading and unloading without the need to depressurize and re-pressurize the growth chamber. Pressures in each chamber is monitored by a MKS instruments baratron and the data is fed back to the HMI. The gate valve between the load lock and the growth chamber is controlled manually using a switch and, to minimize pressure differences, is normally closed during operation.

The main chamber is equipped with several sensing tools, such as a pyrometer, thermocouples both under the heater and close to the substrate holder, a RHEED system, RGA sampling tube and a baratron pressure sensor. The RHEED system is not used during growth due to the relatively high pressures needed for growth. Pressure in the main chamber is controlled by the baratron and a variable throttling valve. This along with the thermocouples and the main heating coil ensures automated control of both pressure and temperature.

The main chamber also houses the hollow cathode plasma source. This plasma source is like that of an capacitively couple RF source operating at 13.56 MHz to a max of 600W, but uses a hollow cathode geometry instead of a parallel plate system. This avoids the need for quartz or glass windows which could potentially add oxygen into the system.[40] In addition to the RF plasma the plasma head can also support DC plasma to a max of 1kV.

The RGA chamber houses the RGA which is separated from the growth chamber by a pneumatic gate valve that can be controlled manually or by the HMI. This valve is normally closed to avoid contamination of the RGA tip. During growth a sampling tube can be lowered into the growth chamber to collect gas which is fed through the top of the RGA chamber. This small opening avoids the risk of contamination of the RGA head.

The gas delivery system is housed inside the gas cabinet and is controlled via the HMI. The system contains all the necessary precursors needed along with bis(cyclopentadienyl)magnesium, a common p-type dopant. Mass flow controllers and pneumatic valves are used to set and control which precursor is allowed into the main vapour line. The valves are activated by an ultra-high purity nitrogen tank (99.9999%) to ensure a lack of contaminations in the lines.

The gas control system can operate very quickly, and allows for very fast binary switching of the precursors. This pulsing of the precursors into the main chamber has been shown to be beneficial to film growth and reduces parasitic vapour phase side reactions that can occur in conventional MOCVD. The timings are controlled by the HMI and are determined by the growth recipe. The system also contains a separate line for the plasma gas. This line has its own flow controller, so delivery of the plasma can be continuously run or pulsed by controlling the voltage at the plasma head.

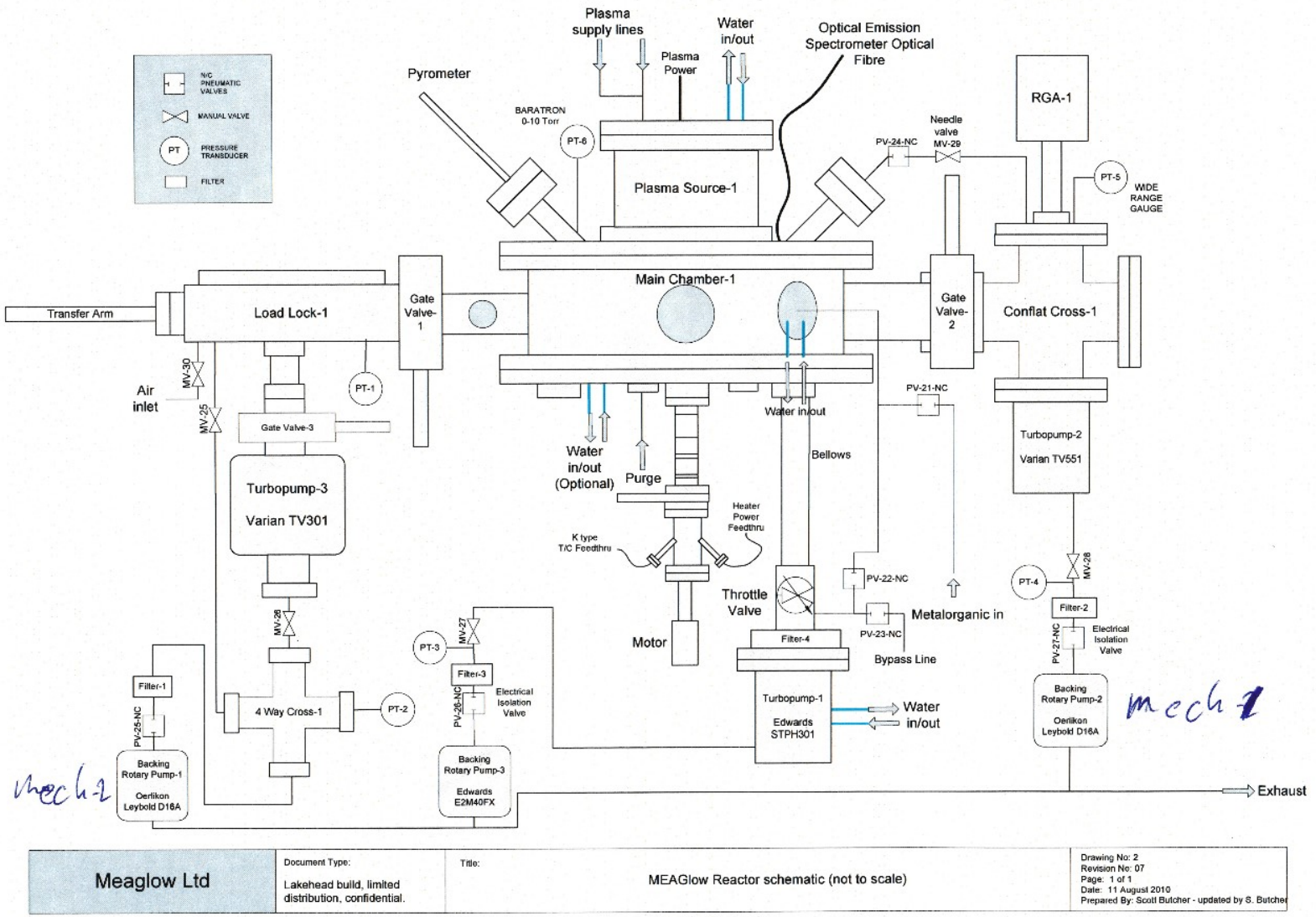


*Figure 15 Schematic for the reactor chamber*

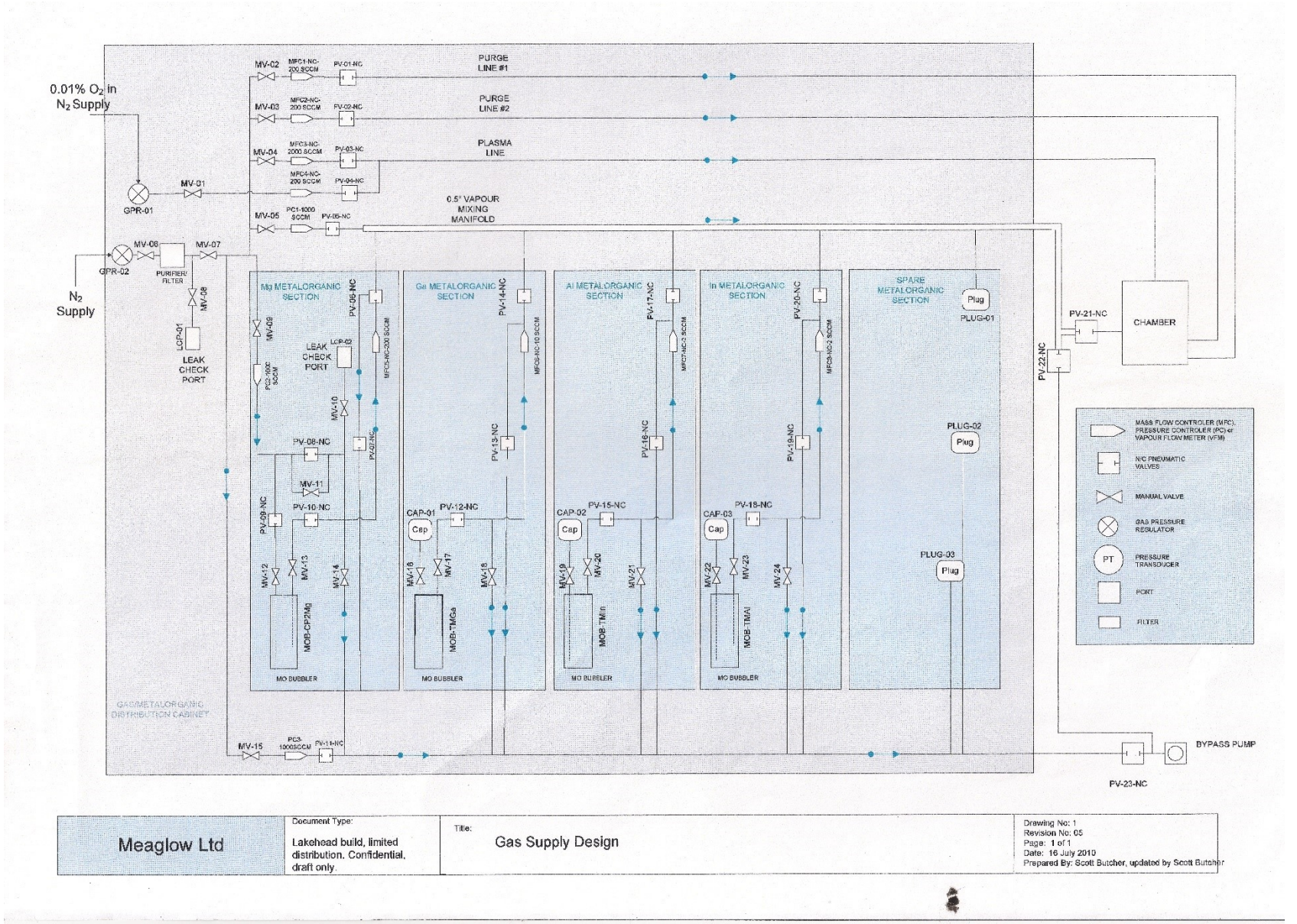


*Figure 16 Schematic of the gas chamber*

# Chapter 5 Results of Experiments and Outcomes

## 5.1 General Growth Procedure

Every growth follows the same procedure:

1. The valve to the RGA chamber is closed to avoid damage/contamination to the filament.
2. Heating in a vacuum at 10°C every 30 seconds.
3. Pressure adjusts to the growing pressure
4. Pre-growth nitridation of the surface at around 600-800W of DC plasma or 100W-600W of RF plasma. The time varied between 1 minute to 30 minutes.
5. Pressure adjustment for growth. Some samples were growth at different pressures then the initial nitridation. As such the system needs time to re-adjust the pressure.
6. The precursor valve is opened to the vapour line to have no lag time between the pluses.
7. The precursor is pulsed into the chamber. For the growth of InN, the plasma is also turned on in this step, as the plasma runs continuously during growth. This technique is called metal modulated epitaxy and was found to be beneficial for the growth of InN. For GaN and AlN the plasma was off for this step to avoid the formation of nitride powders. Flow rates for the precursors were taken from previous growths.
8. Pulse of nitrogen plasma. The pressure in the main chamber is maintained using the plasma line. When plasma is needed a bias is applied to the plasma head (DC or RF). During this time the metal organic precursor is sent to the bypass line.
9. A small nitridation is needed between loops (around every 20 cycles) for InN for prevention of surface droplets. GaN and AlN do not need this step.
10. Step 7, 8 and 9 are repeated. This is a single cycle. Thickness of the layer depends greatly on the number of cycles used for the growth.

11. All gases are turned off and cooling begins under a vacuum. The cooling is done at the same rate as the heating, however since the system is air-cooled the cooling curve is not linear samples are typically removed at temperatures between 30°C and 100°C.
12. RGA chamber valve is opened when the cool down has finished.

## 5.2 Growth Preparation

The sample holder was cleaned using abrasives before deposition of different materials to avoid cross-contamination of the grown samples. The abrasives used were a combination of metal sand papers ranging in grits from 80 grit to 180 grit, acetone and deionized water were used as the lubricant during sanding to remove old nitride particles. The substrates were cleaned using acetone then ethanol and were placed under vacuum in the load lock. Transfer from the load lock to the growth chamber is done using a magnetically coupled loading arm and a view port on the side of the reactor.

## 5.3 Silicon Carbide Substrates

The silicon carbide templates were commercially purchased from Silicon Quest. The substrates are initially 2” in diameter which are broken up into smaller pieces (typically 1cm x 1cm) for growth to maximize the amount of growths which can be done per wafer. Elemental analysis done on the substrates show a layer of silicon, silicon carbide and finally a layer of gallium nitride.

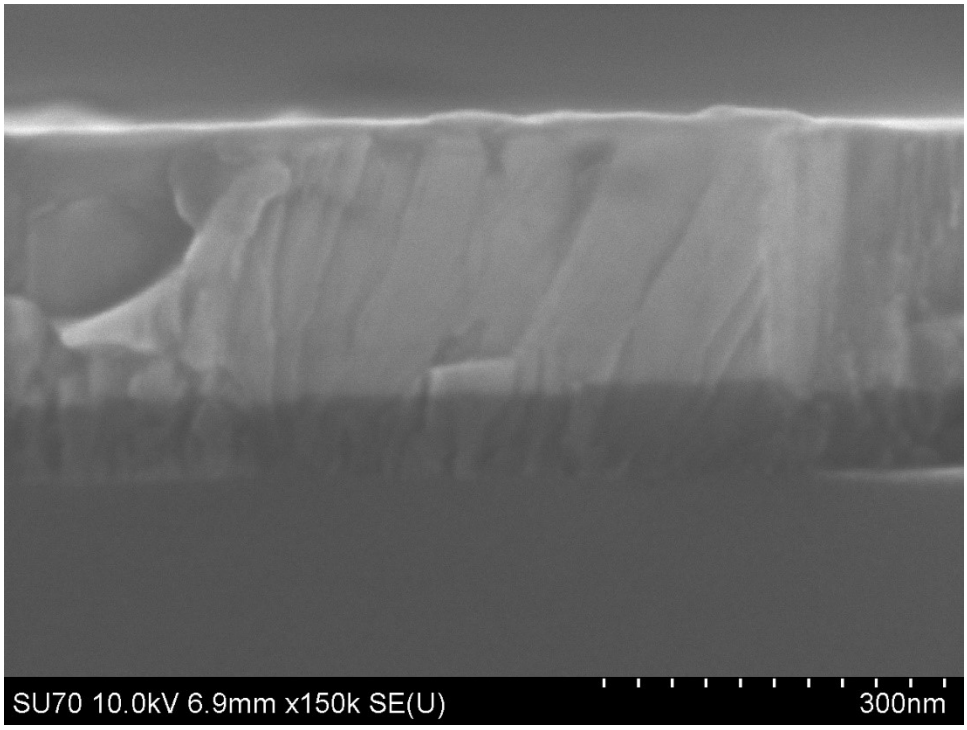


*Figure 17 SEM image of the SiC Template The light grey area is the GaN and the dark great area is SiC, under the SiC is silicon*

To determine the type of silicon carbide in the substrate a wet etch of the gallium nitride was performed. The substrate was placed in a solution of 3M KOH (potassium hydroxide) and 0.02M of $K_2S_2O_8$ (potassium persulfate) illumined by a deuterium lamp and heated to 80°C for 2 hours or until visually the GaN layer was removed (since the GaN layer etched off in pieces this visual inspection was possible). [41] The etch will remove the GaN layer but leave the Si and SiC layer untouched. XRD measurements were then made to determine the orientation of the SiC. Figure 18 shows the XRD plot of the SiC template before and after the etch. The GaN peak disappears and what is left is the SiC at 35.77°. This peak is small in comparison to the GaN peak as the thickness of the SiC layer is around 70nm while the GaN layer is around 250nm. Roughness measurements were also done during the etching to determine if the etch was having an effect. Figure 19 shows the before and after AFM scans (a and b respectively), the RMS roughness before the etch was 10.92 nm and after the etch the roughness was found to be 3.91 nm.

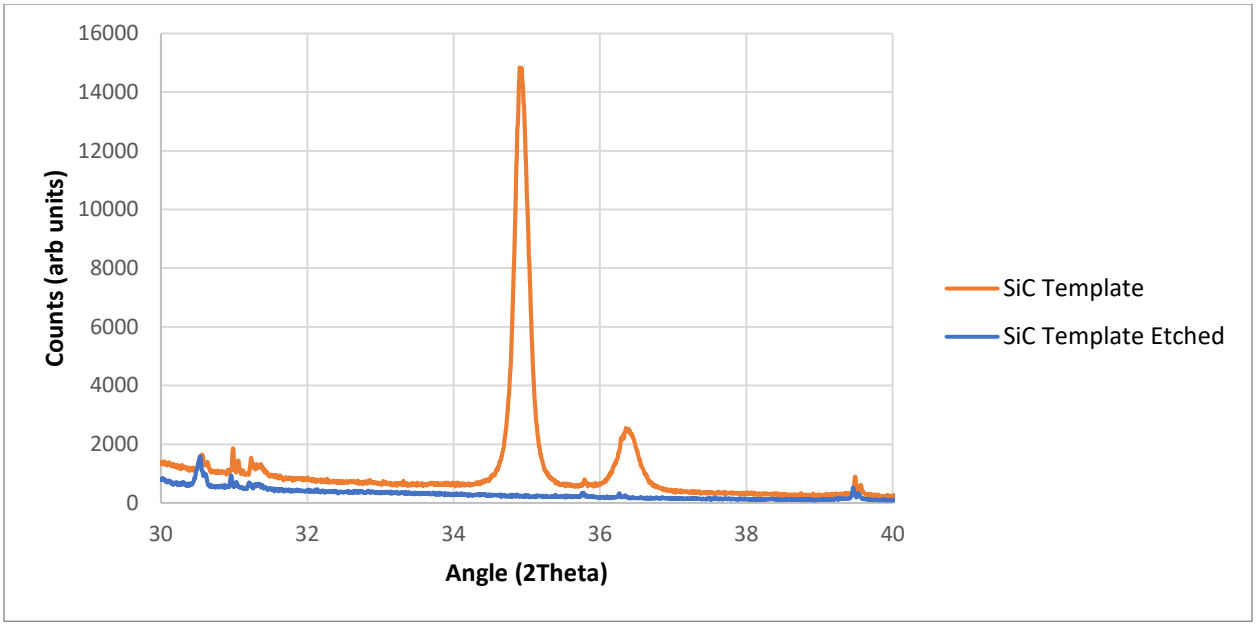


*Figure 18 XRD plot of the template vs the etched template after removal of all the GaN*

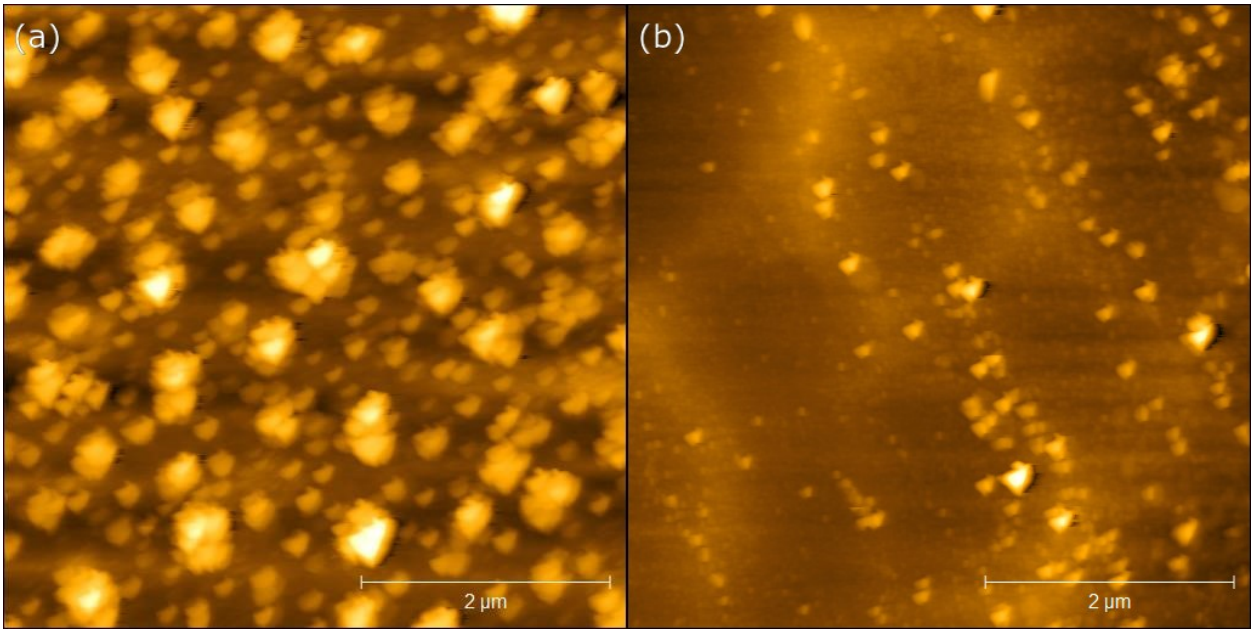


*Figure 19 (a)SiC template before etching (b)SiC Template after etching*

## 5.4 Aluminum Nitride Results

Attempts to grow AlN were proven to be unsuccessful, with results showing only the underlying substrate in the XRD data. A summary of growths can be seen in Table 13.

A multitude of growth techniques were used to try and grow AlN on the substrates. Three different types of growths techniques were used to try and obtain AlN. First was a direct MOCVD

technique with just pulsing of the aluminum precursor then a pulse of RF nitrogen plasma. For growths 18 and 19, magnesium and gallium, respectively were added to act as a surfactant [42]. This had no effect on the growth.

The second growth technique was a type of modified atomic layer deposition (ALD) technique. In this technique the AlN is pulsed into the chamber while the valve is closed, and some time is given to allow the aluminum to settle. Then the valve is opened, and any unreacted precursor is vacuumed out. Then the pressure is established for the plasma and is pulsed. The idea was to try to only convert settled aluminum into AlN.

The third and final technique tried was a metal modulated technique. This technique is shared with InN, in that the plasma is constantly running along with a wait step. One cycle of growth is as follows

1. 20 cycles of metal modulated AlN is deposited with the parameters of growth 2 and 3 in
2. A 25 second plasma nitridation step to force any unreacted precursor to react.
3. Loop back to 1.

This process was to try and force the precursor to react with the nitrogen plasma instead of any of the methyl group that was split off from the precursor. From the stated three techniques, the technique with the most promise was the direct MOCVD technique and this was used in the creation on InAlN. Another technique used to assist in growing the AlN was the use of a low temperature AlN buffer layer. 50 cycles of AlN were deposited at a lower temperature then the growth temperature to try and deposit amorphous AlN nucleation sites. [43]

SEM results from growths 3, 8, 17 and 21 can be seen in Figure 20. From here it can be seen that in growths 3 and 8, there was a diffusion between the GaN layer and the AlN layer. This is confirmed by the EDX in Figure 21 and Figure 22 and from the thicknesses. The layer is thicker

than the initial GaN layer, which means there was growth. How much growth is not apparent as the actual thickness of the underlying GaN layer varies across the wafer. In growth 17, however there was an apparent layer of AlN grown, separate from the GaN layer. The EDX in Figure 23 for the layers confirms that elemental aluminum and nitrogen are present. Finally, in growth 21 a very thick layer of aluminum metal was deposited. This was caused by too much TMA precursor and not enough nitrogen plasma to convert the metal to AlN. Figure 25 shows the AFM scans of the growths, the RMS roughness is (a) 9.293 nm, (b) 4.274 nm, (c) 4.408 nm and (d) 84.30 nm for growths 3, 8, 17 and 21 respectively. Growths 8 and 17 were grown using ALD (8) and straight MOCVD with DC plasma (17), which had a similar roughness even though there was diffusion in growth 8. This was because of the slow growth from ALD which caused a more uniform layer to form. As expected from the SEM image and corresponding EDX growth 21 was very rough due to the coalescing of the aluminum layer. Growth 3 shows some improvement from the initial GaN layer which shows the growth becoming smoother over time.

AlN growths were subjected to XRD scanning for verification. Since the x-rays penetrate to the silicon layer in the substrate, all the peaks are relative to that silicon peak. To view this better the XRD graphs are plotting on a log scale and zoomed in to the 30°-40° area of interest. Because of the high silicon peak and GaN peaks, any AlN peaks would be lost to noise unless they were of very high quality. Figure 26 AlN XRD Plots shows the XRD plots of the growths along with the substrate for reference. There is no apparent AlN peak despite there being a layer of AlN in growth 17. This means that the AlN is of poor quality or amorphous and further research is required to verify the AlN layers.

Raman and Hall effect measurements were attempted but no concise results could be collected.

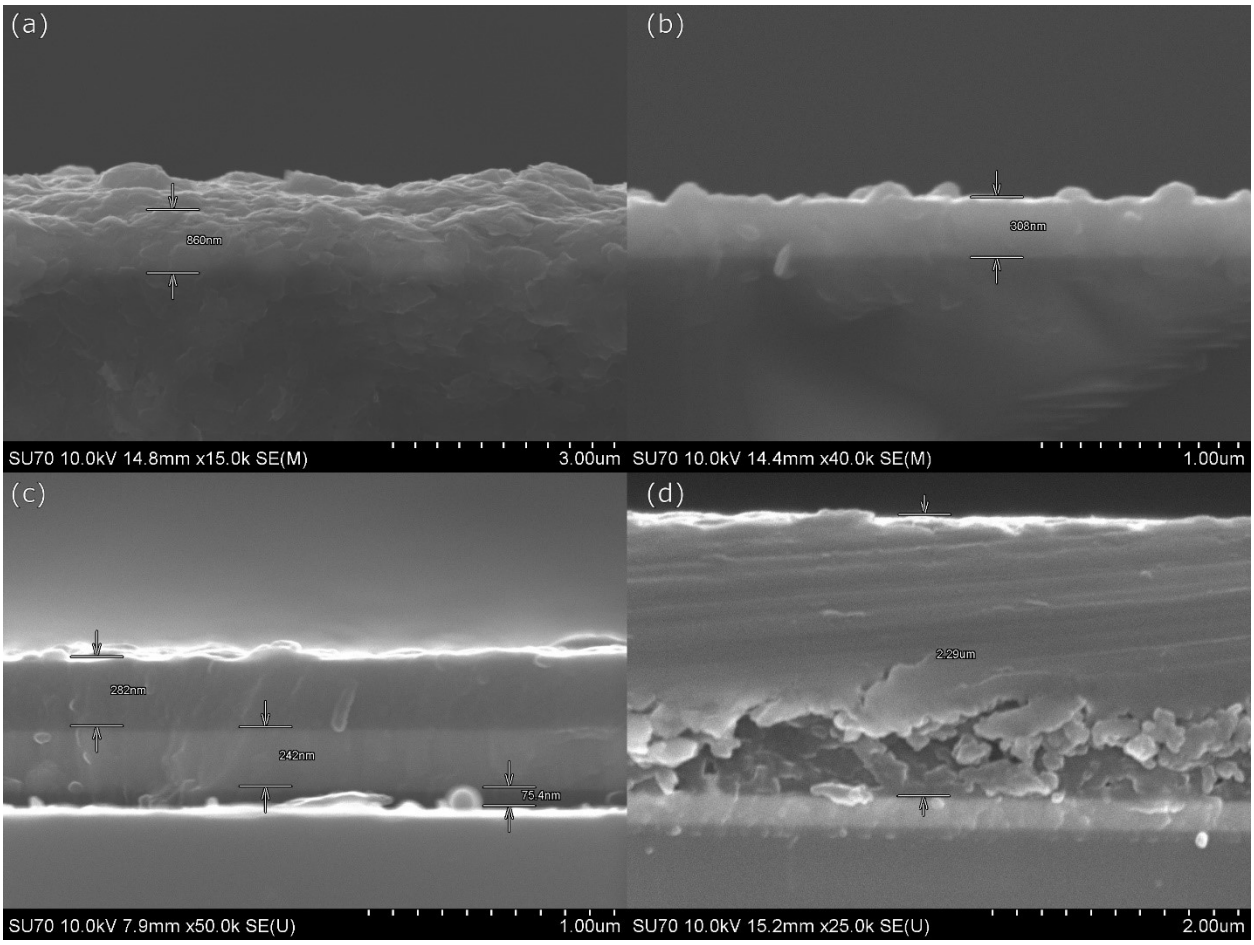


*Figure 20 SEM images with thickness measurements for (a) Growth 3, (b) Growth 8, (c) Growth 17 and (d) Growth 21*

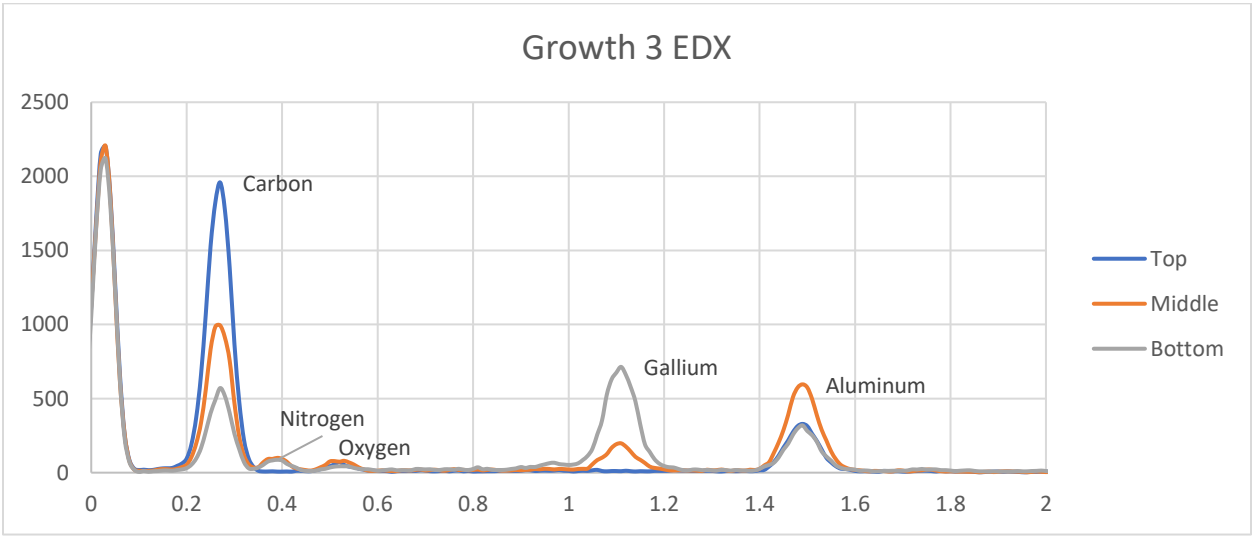


*Figure 21 EDX graph for growth 3*

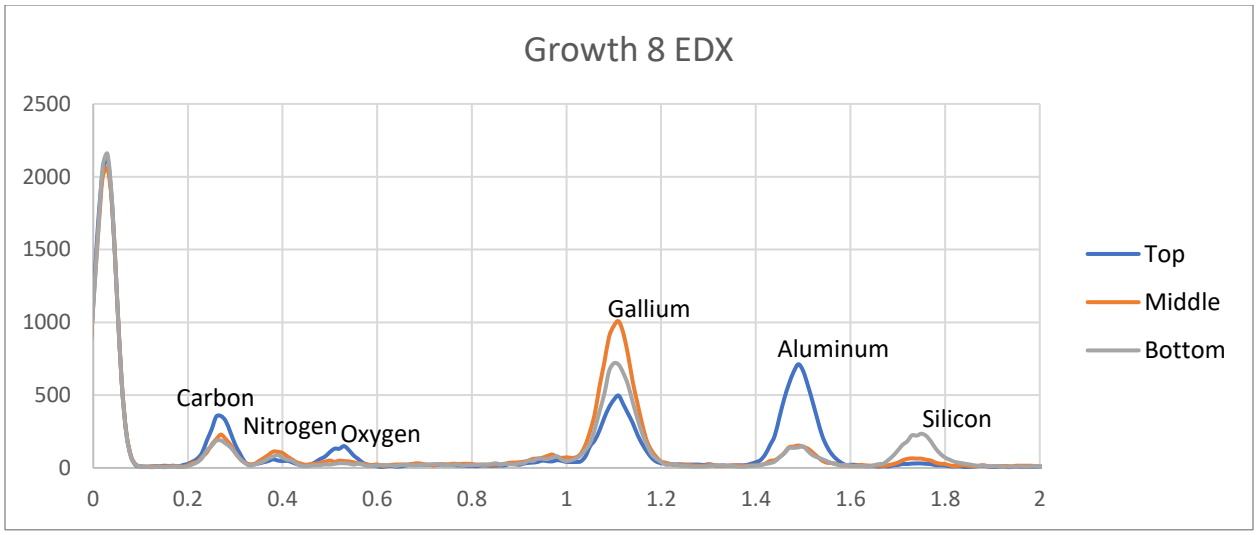


*Figure 22 EDX graph for growth 8*

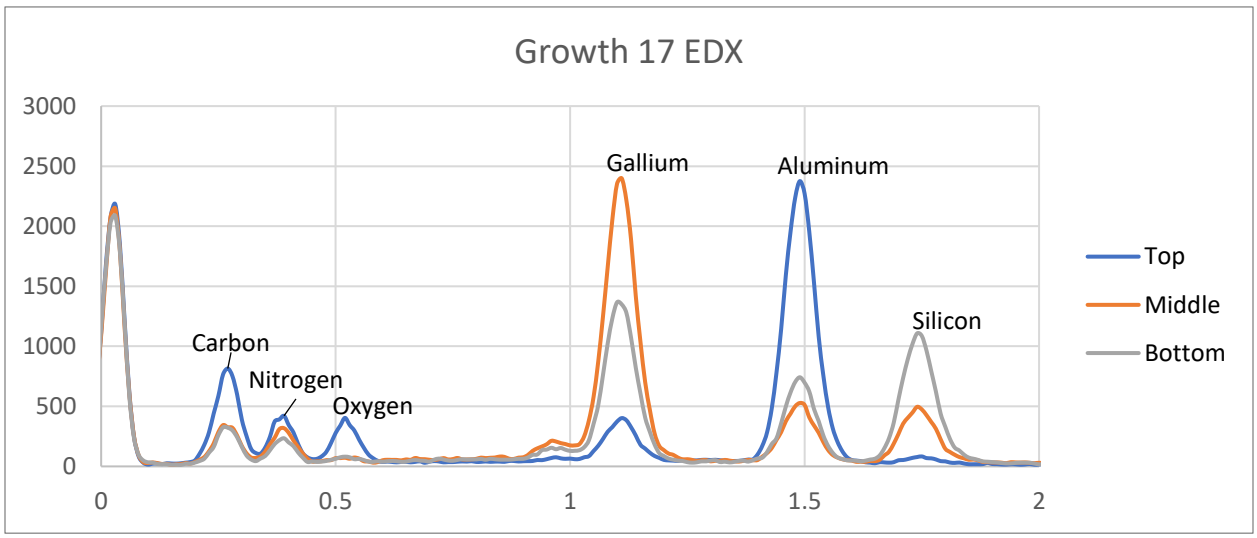


*Figure 23 EDX graph for growth 17*

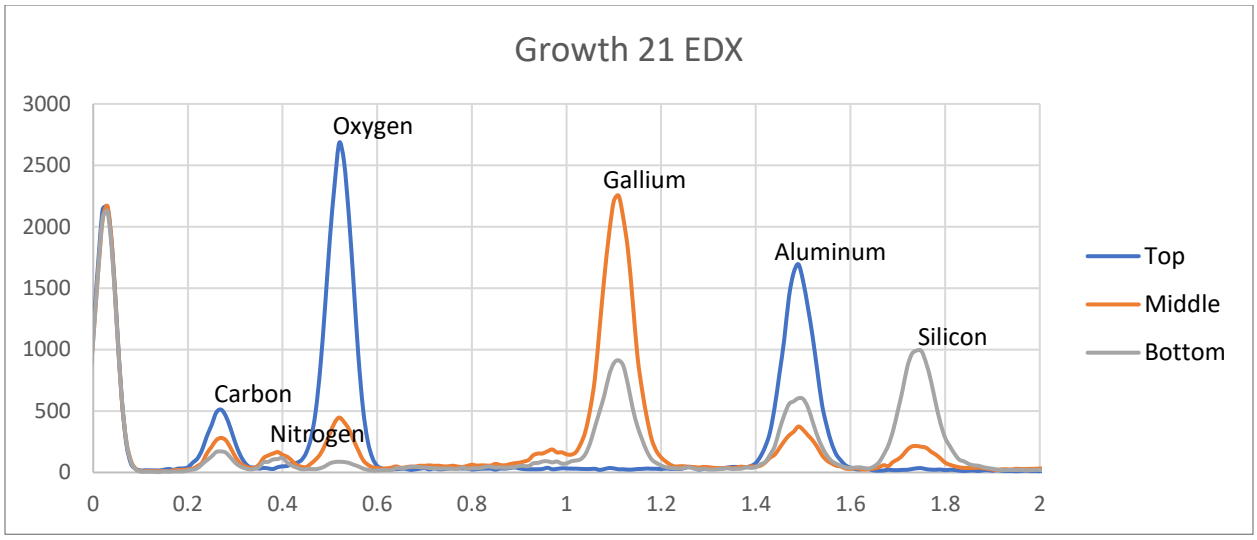


*Figure 24 EDX graph for growth 21*

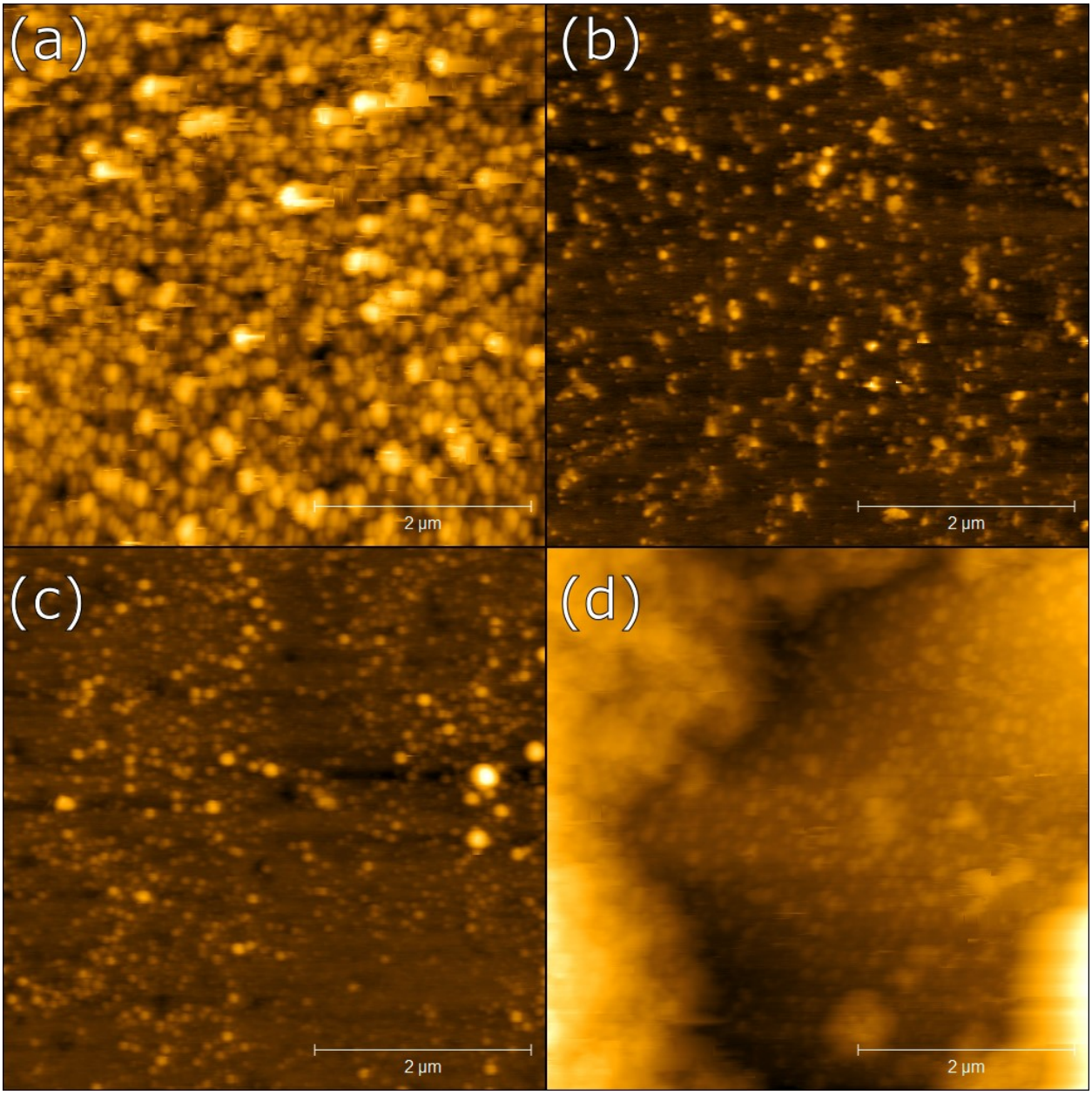

*Figure 25 AFM scans of (a) Growth 3, (b) Growth 8, (c) Growth 17 and (d) Growth 21*

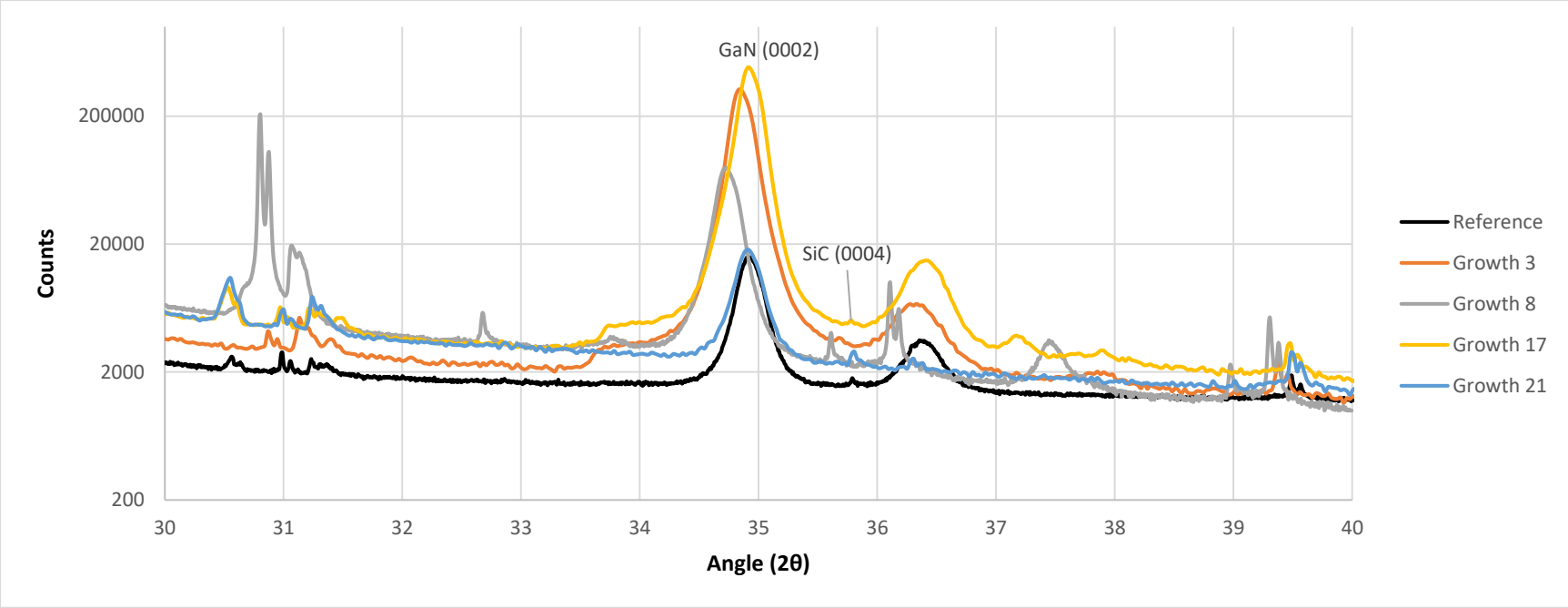


*Figure 26 AlN XRD Plots*

*Table 13 Summary of growth parameters for AlN*

| Growth Number | MO Ratio | Plasma Type | Plasma Power | Plasma Pressure (mTorr) | Temperature (°C) | RPM | Cycles | Nitridation Time (s) | Nitridation Power | Nitrogen Pressure (mTorr) | Technique |
|---|---|---|---|---|---|---|---|---|---|---|---|
| **1** | 1.25 | RF | 600W | 750 | 540 | 60 | 400 | 60 | 600W | 750 | MOCVD |
| **2** | 1 | RF | 600W | 750 | 540 | 60 | 400 | 60 | 100W | 750 | Metal Modulated |
| **3** | 1 | RF | 600W | 750 | 540 | 20 | 800 | 60 | 100W | 750 | Metal Modulated |
| **4** | 0.2 | RF | 300W | 300 | 540 | 30 | 180 | 60 | 100W | 700 | ALD |
| **5** | 0.1 | DC | 400V | 300 | 540 | 30 | 180 | 60 | 400V | 300 | ALD |
| **6** | 0.1 | DC | 400V | 300 | 540 | 30 | 200 | 900 | 800V | 300 | ALD |
| **7** | 0.1 | DC | 400V | 300 | 540 | 30 | 200 | NA | NA | NA | ALD |
| **8** | 0.1 | DC | 600V | 300 | 540 | 30 | 250 | 900 | 800V | 300 | ALD |
| **9** | 0.1 | DC | 600V | 650 | 540 | 30 | 200 | 900 | 800V | 650 | ALD |
| **10** | 0.1 | DC | 1000V | 300 | 540 | 30 | 200 | 900 | 1000V | 300 | ALD |
| **11** | 1.2 | DC | 1000V | 300 | 540 | 30 | 200 | 900 | 1000V | 300 | ALD |
| **12** | 1 | DC | 800V | 250 | 540 | 30 | 600 | NA | NA | NA | MOCVD |
| **13** | 0.5 | DC | 800V | 250 | 540 | 30 | 600 | NA | NA | NA | MOCVD |
| **14** | 0.5 | DC | 700V | 250 | 540 | 30 | 600 | NA | NA | NA | MOCVD |
| **15** | 0.5 | DC | 900V | 250 | 540 | 30 | 600 | NA | NA | NA | MOCVD |
| **16** | 0.5 | DC | 800V | 250 | 540 | 30 | 600 | NA | NA | NA | MOCVD |
| **17** | 0.5 | DC | 800V | 250 | 540 | 30 | 1200 | NA | NA | NA | MOCVD |
| **18** | 0.5 | DC | 800V | 250 | 540 | 30 | 600 | NA | NA | NA | Mg Surfactant |
| **19** | 0.5 | DC | 800V | 250 | 540 | 30 | 600 | NA | NA | NA | Ga Surfactant |
| **20** | 0.5 | DC | 800V | 250 | 540 | 30 | 600 | 900 | 800V | 250 | AlN Buffer |
| **21** | 0.5 | DC | 800V | 250 | 540 | 30 | 800 | 900 | 800V | 250 | AlN Buffer |

## 5.4 Gallium Nitride Results

GaN growths were difficult to detect as the substrate itself contains GaN as a layer. Generally, when trying to determine if there was any growth, there are a few things to consider. 1) Is the FWHM better than the substrate. If so, then there is growth that made a better crystal. 2) What is the RMS roughness of the surface. If the surface is smoother, either thermal annealing or growth has happened. 3) Did the relative height of the XRD peak change. This means, typically, a thicker layer but could also mean a layer of higher crystallinity.

Growth of GaN on the substrates was performed using a few different techniques. First was a direct MOCVD method using AlN as a buffering layer. This was done before the GaN layer on the substrate was discovered. This AlN was grown both using a direct MOCVD technique and a combination of ALD and MOCVD (done only in growth 12). Both RF and DC plasmas were used to a varying degree of success. In addition to the AlN buffer layer, a low temperature GaN layer was deposited before the proper GaN layer was grown. This was done for growths 13, 15, 16, 18 and 20. Growths 17 and 29 were grown as very thick layers, with multiple growths being performed upon the same substrate.

XRD results can be seen in Figure 32 GaN XRD Plots, as stated above to determine if there was growth one of the ways is the FWHM of the XRD graph, in addition the peak position of the XRD (which designates the type of crystal grown) this is summarized in Table 14 for the plots shown in Figure 32. The peak shift is due to both strain on the GaN layer and from the x-rays being reflected on a higher z-axis than what the XRD detector is looking for.

*Table 14 XRD peak positions and FWHM for the reference and selected growths*

| Growth | Peak Position(°) | FWHM(°) |
|---|---|---|
| Reference | 34.903 | 0.229 |
| 10 | 34.834 | 0.181 |
| 11 | 34.833 | 0.187 |
| 15 | 34.806 | 0.255 |
| 19 | 34.797 | 0.202 |

AFM measurements performed on growth 10 and growth 19 can be seen in Figure 27. Growth 19 (a) had an RMS roughness of 8.646nm while growth 10 (b) had an RMS rougness of 3.928 nm. Both growths had similar growth recipies with only differencing being RF (growth 10) to DC (growht 19) plasma and an AlN buffer to a GaN buffer layer.

Raman measurements were done on the substrate and growth 19 and can be seen in Figure 28. From the results, the $E_2$ peak on the substrate is unstrained at 565.42 $cm^{-1}$. On the growth the $E_2$ peak is reduced, which would indicate that the crystal quality of the growth is less than that of the substrate. However, the FWHM of the XRD peak being smaller indicates a higher crystal quality. Therefore, the results of the grown layer are inconclusive as to the grown layer being of higher quality. In addition, the $A_1$(LO) peak seen in the spectra on the grown layer indicates a higher carrier concentration caused by doping. This is probably due to oxygen or carbon contamination in the chamber during growth.

SEM measurements were performed on growths 10 and 19. The results of which can be seen in Figure 29. Because the substrate has GaN on top of the SiC the thickness measurements include the base layer as well as the grown layer. As such the actual thickness of the grown layer can only be approximated, with growths 10 being around 130nm and growth 19 being 240nm thick.

EDX measurements were performed for completeness as EDX can only provide an elemental analysis and GaN was already confirmed to be on the substrate.

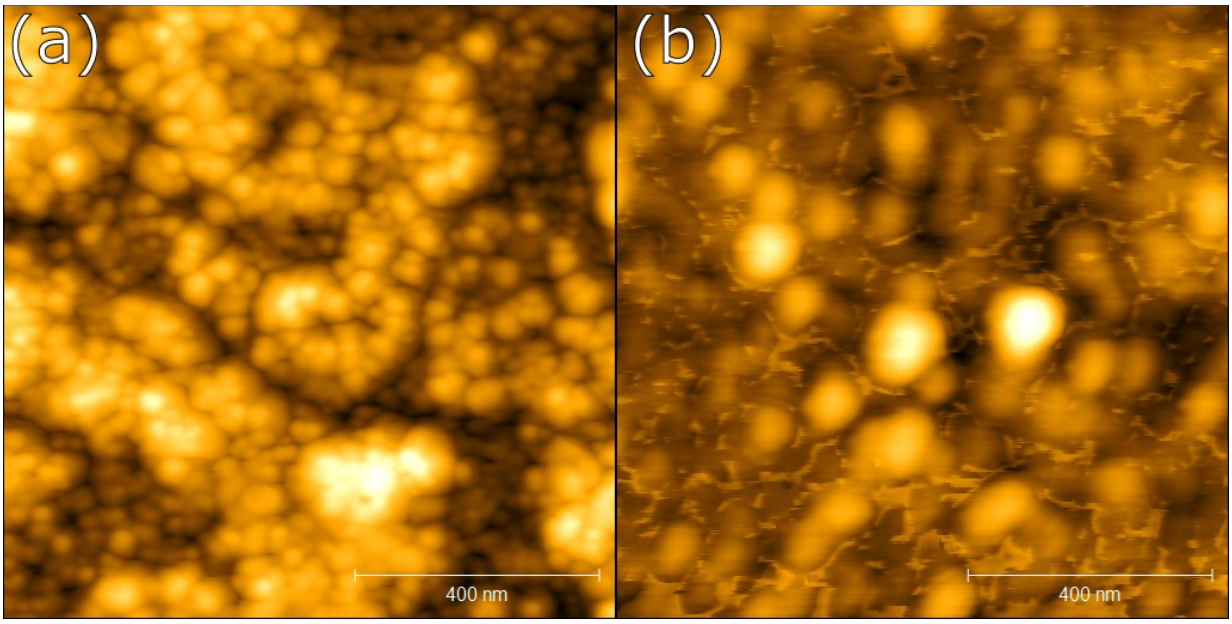


*Figure 27 AFM Measurements for GaN (a) Growth 19, (b) Growth 10*

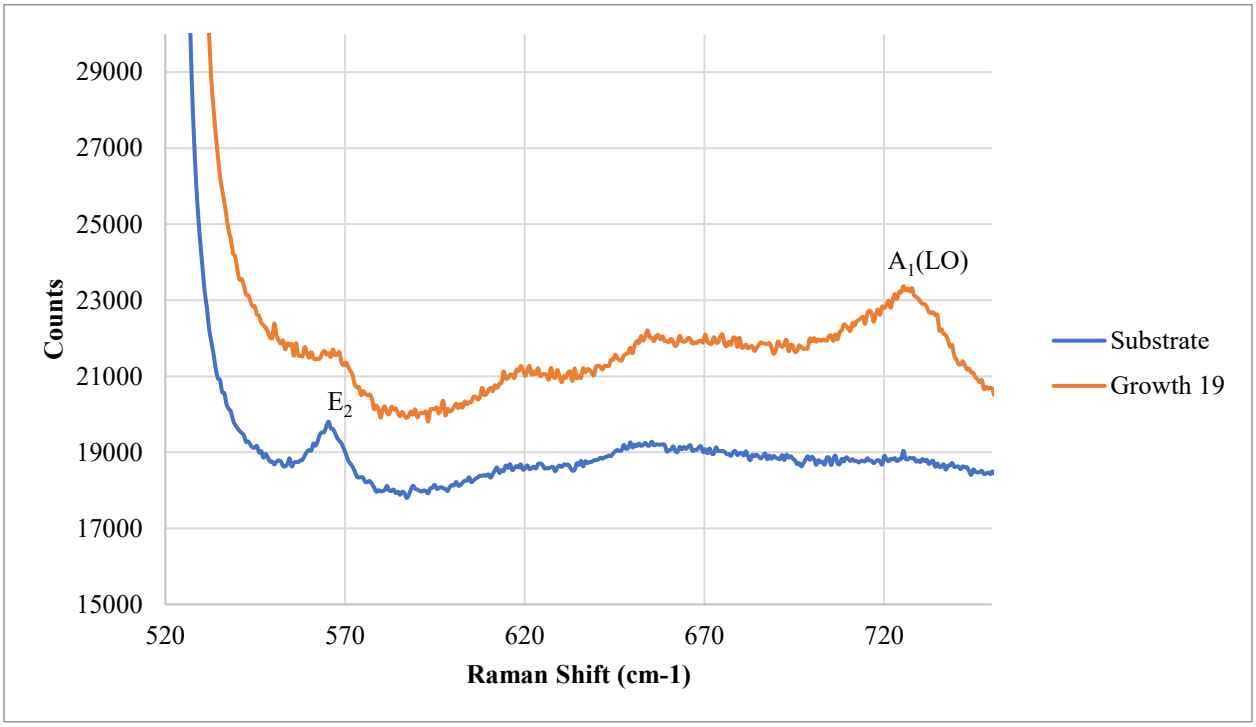


*Figure 28 Raman measurements for growth 19 as compared to the substrate*

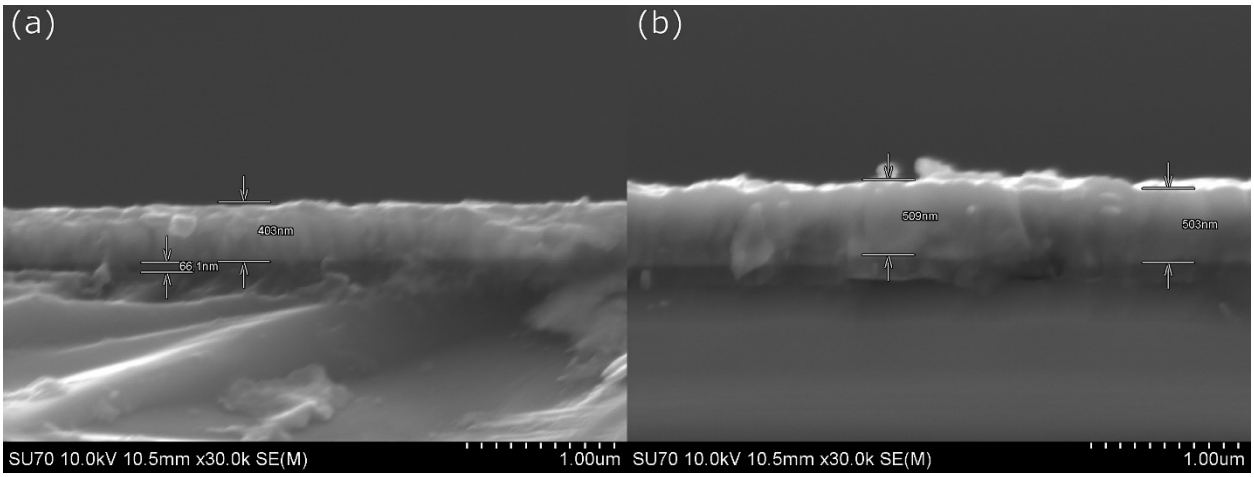


*Figure 29 SEM results for GaN (a) growth 10 (b) growth 19.*

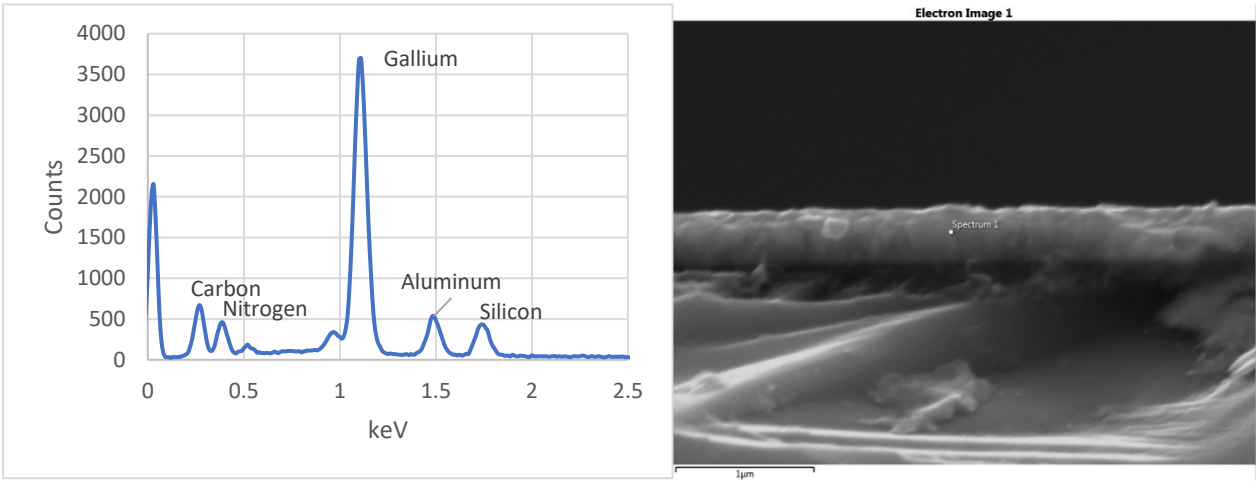


*Figure 30 EDX measurement for growth 10 with the corresponding SEM image*

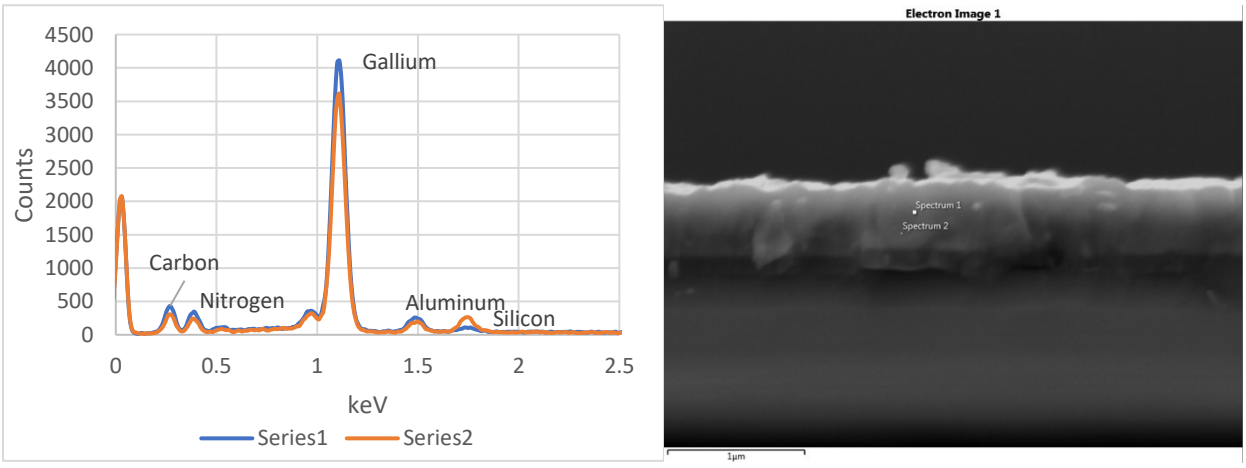


*Figure 31 EDX measurements for growth 19 with the corresponding SEM image*

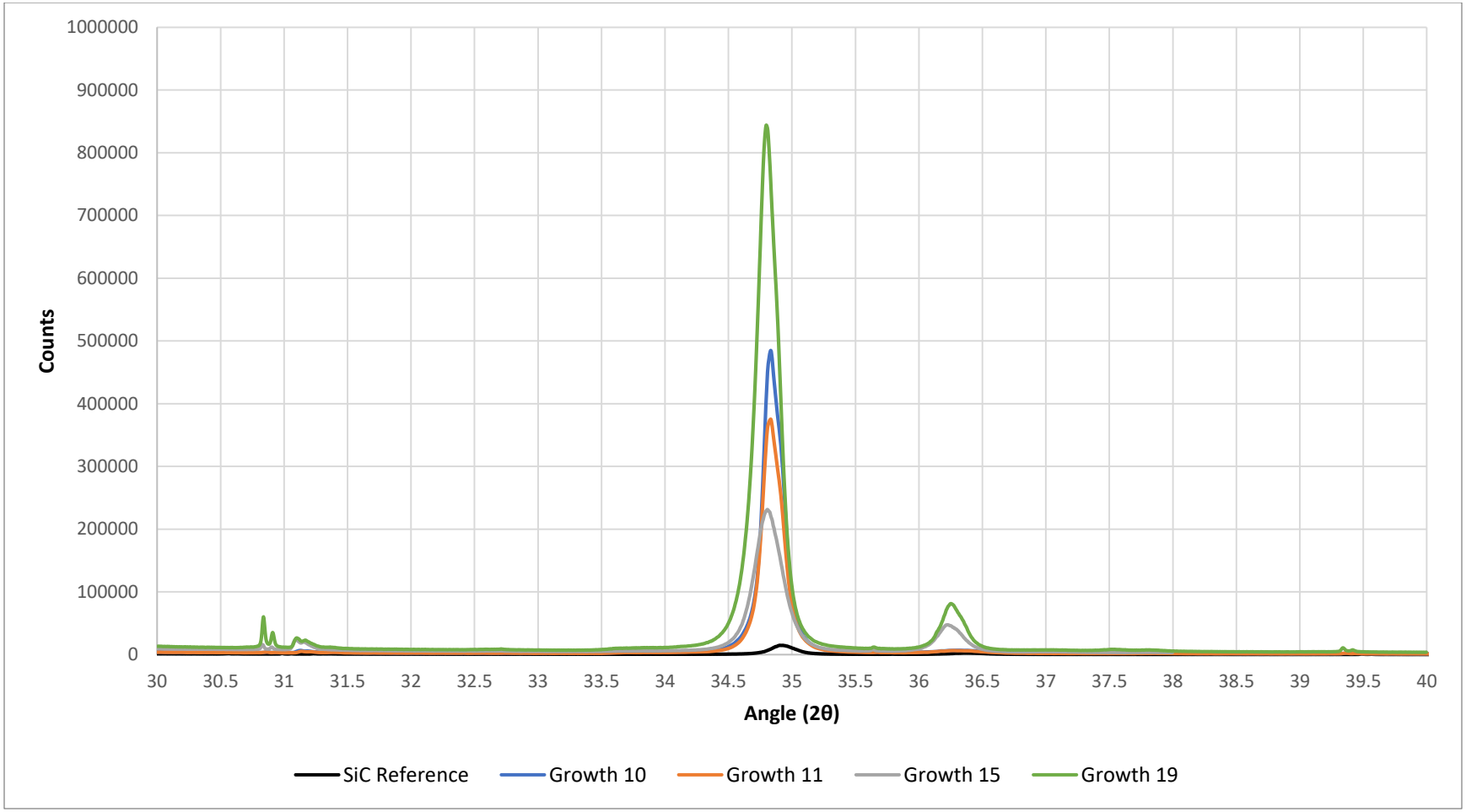


*Figure 32 GaN XRD Plots*

*Table 15 GaN growth summary*

| Growth Number | MO Ratio | Plasma Type | Plasma Power | Plasma Pressure (mTorr) | Temperature (°C) | RPM | Cycles | Nitridation Time | Nitridation Power | Nitrogen Pressure (mTorr) | Buffer Layer | Buffer layer Cycles |
|---|---|---|---|---|---|---|---|---|---|---|---|---|
| **1** | 0.5 | RF | 600W | 1200 | 445 | 60 | 150 | 600 | 600W | 750 | AlN | 150 |
| **2** | 0.5 | RF | 600W | 1200 | 445 | 20 | 450 | 600 | 600W | 750 | AlN | 300 |
| **3** | 0.69 | RF | 600W | 750 | 540 | 60 | 400 | 60 | 600W | 750 | AlN | 100 |
| **4** | 0.54 | RF | 600W | 750 | 540 | 60 | 400 | 60 | 600W | 750 | AlN | 100 |
| **5** | 0.5 | RF | 600W | 1200 | 445 | 20 | 600 | 600 | 600W | 750 | AlN | 150 |
| **6** | 0.5 | RF | 600W | 1200 | 445 | 20 | 600 | 600 | 600W | 750 | AlN | 100 |
| **7** | 0.5 | RF | 600W | 1200 | 445 | 20 | 600 | 600 | 600W | 750 | AlN | 50 |
| **8** | 0.5 | RF | 600W | 1200 | 540 | 20 | 600 | 600 | 600W | 750 | AlN | 100 |
| **9** | 0.5 | RF | 600W | 1200 | 540 | 20 | 600 | 600 | 600W | 750 | AlN | 100 |
| **10** | 0.5 | RF | 600W | 1200 | 540 | 20 | 1200 | 600 | 600W | 750 | AlN | 100 |
| **11** | 0.5 | RF | 600W | 1200 | 445 | 60 | 600 | 600 | 600W | 750 | AlN | 100 |
| **12** | 0.5 | RF | 600W | 1200 | 445 | 60 | 600 | 600 | 600W | 750 | AlN | 20 ALD + 100 direct |
| **13** | 0.5 | DC | 600V | 350 | 540 | 60 | 900 | 1800 | 600V | 350 | GaN | 100 |
| **14** | 0.5 | DC | 600V | 350 | 540 | 60 | 900 | 1800 | 600V | 350 | AlN | 100 |
| **15** | 0.5 | DC | 800V | 350 | 540 | 60 | 900 | 1800 | 800V | 350 | GaN | 100 |
| **16** | 0.5 | DC | 800V | 350 | 540 | 60 | 900 | NA | NA | NA | GaN | 100 |
| **17** | 0.5 | DC | 800V | 350 | 540 | 60 | 1500 | NA | NA | NA | NA | NA |
| **18** | 0.5 | DC | 800V | 350 | 540 | 60 | 900 | NA | NA | NA | GaN | 100 |
| **19** | 0.5 | DC | 800V | 350 | 540 | 60 | 1500 | NA | NA | NA | NA | NA |
| **20** | 0.5 | DC | 800V | 350 | 540 | 60 | 2700 | NA | NA | NA | GaN | 100 |

## 5.5 Indium Nitride and Indium Aluminum Nitride Results

Indium nitride was attempted to be grown on the SiC template. However, initial growths formed a white powder on the surface of the substrate, which is indicative of indium metal being formed and not adhering to the substrate surface. It was only when the InN was used in conjunction with aluminum nitride was any form of InN peak visible in the XRD and a smooth layer formed on the surface of the substrate. The InAlN growths only show the InN peaks, and since no band gap measurements were made on the samples, due to the lack of measuring devices at Lakehead, only the InN can be considered when analyzing the data. Growths 10 to 19 have a 300-cycle layer of AlN used as a capping layer. This layer is not listed in Table 19 as there was no AlN peak detected and was assumed to not be crystalline. It would however show in in the AFM scans.

AFM results can in seen in Figure 33 and the corresponding RMS roughness are in Table 16. Growth 11 has a smaller InN buffer layer of the three and growth 16 and 17 are the same aside from the AlN capping layer in growth 17, which has 50 cycles grown at the maximum temperature to try and encourage AlN growth.

*Table 16 AFM RMS roughness for the listed growths*

| Growth Number | RMS Roughness (nm) |
|---|---|
| **11** | 11.31 |
| **16** | 17.18 |
| **17** | 17.62 |

XRD scans on just pure InN can be seen in Figure 37. From the plots there is no apparent InN peak just peaks associated with the substrate. Figure 38 shows the XRD scans of InAlN which shows the InN peak. However, just like in the pure InN growths there is a layer of indium metal. To determine if the metal is within the layer or on top, an XRD scan of growth 19 was done at both room temperature (25°C) and above the melting point of indium (170°C), the results can be seen in Figure 39, at room temperature the indium peak is present, while at 170°C the peak is gone.

This indium metal is caused by the increase in growth temperature causing desorption of the indium from the InN layer. [44]

In some of the XRD results there looks to be a secondary peak within the (0002) InN peak. This peak corresponds to the $k\alpha_2$ doublet which normally overlaps the $k\alpha_1$ peak at low angles but, can be seen sometimes.

*Table 17 InAlN XRD results for selected growths*

| Growth | Peak Position(°) | FWHM(°) |
|---|---|---|
| 11 | 31.525 | 0.275 |
| 13 | 31.599 | 0.220 |
| 16 | 31.68 | 0.160 |
| 17 | 31.67 | 0.152 |
| 18 | 31.699 | 0.170 |

SEM images of growths 11 and 16 can be seen in Figure 34. Growth 11 does not show the multiple layers of InN-InAlN-AlN that growth 16 shows (it should be noted that the AlN capping layer is not AlN, it is aluminum metal as per the EDX measurement), even though it has the same recipe structure.

Varying the In/Al ratio was also attempted to see if the increased Al would have any effect on the growth. Growths 6,7, and 8 all correspond to this attempt. There was no noticeable AlN peak, even with a 25/75 ratio. As such a 50/50 ratio was kept as the standard recipe.

Raman and Hall effect measurements were attempted but no concise results could be collected.

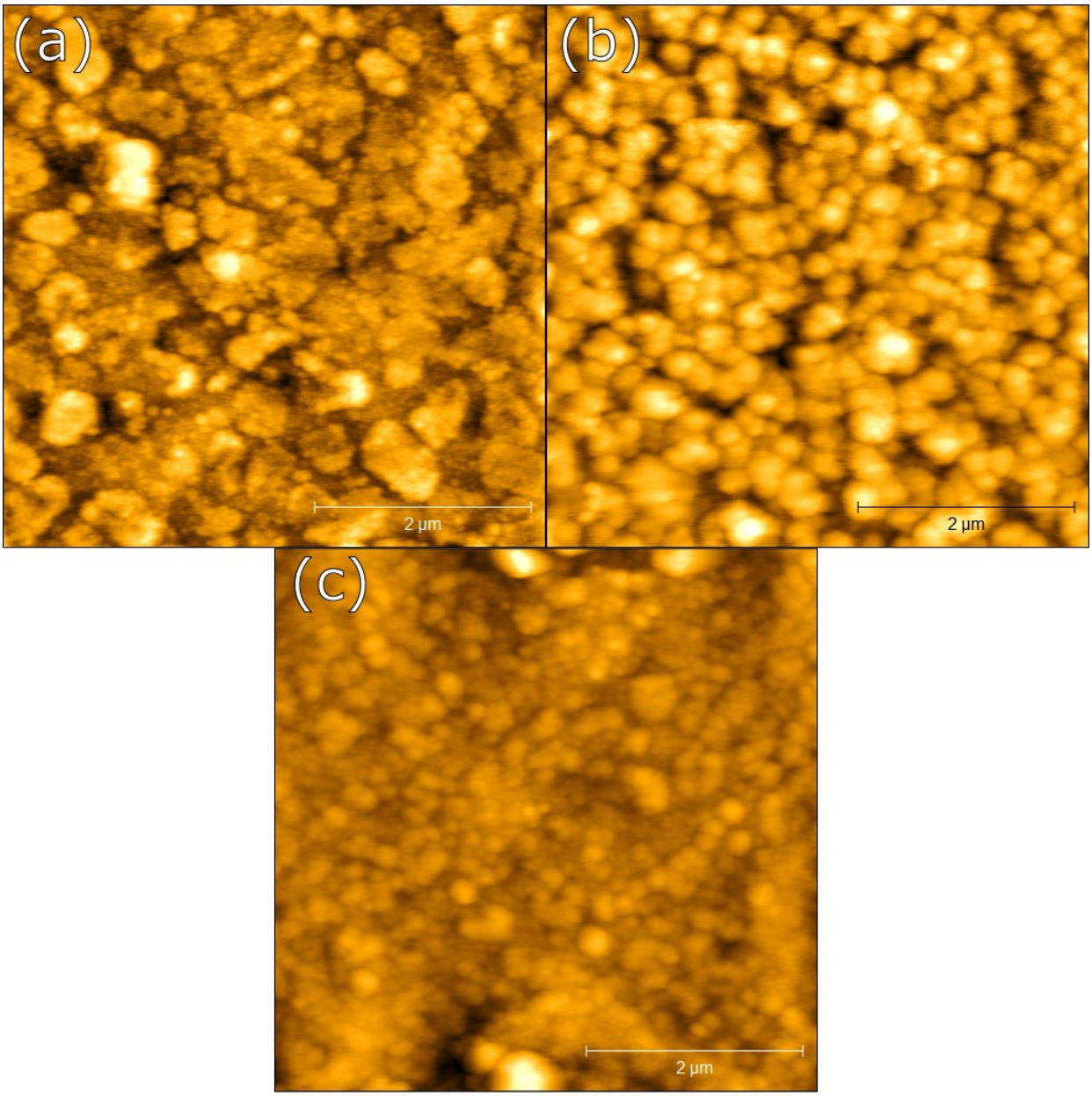


*Figure 33 AFM images for (a) growth 11, (b) growth 16 and (c) growth 17*

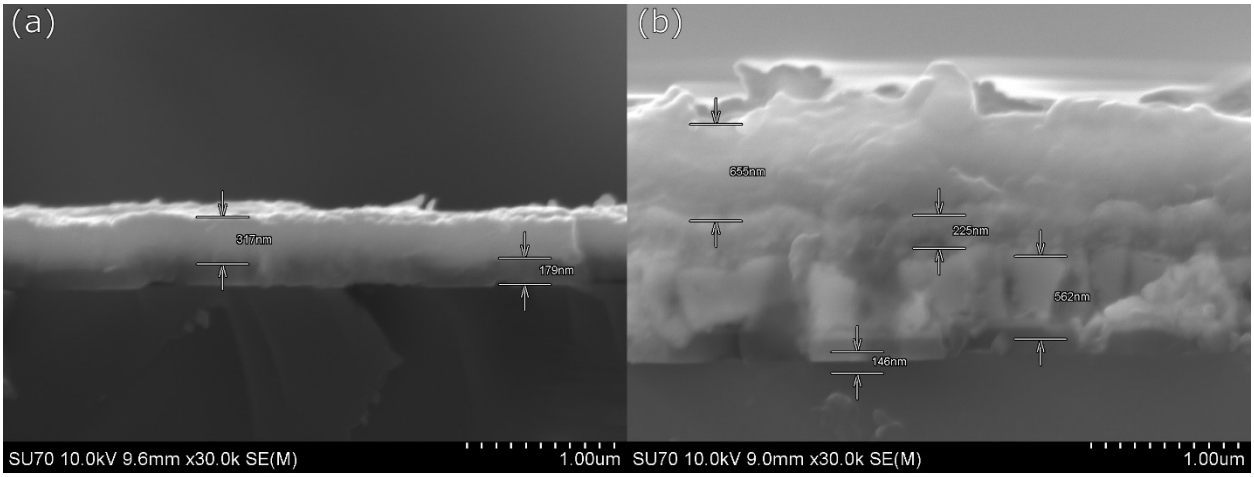


*Figure 34 SEM images for InAlN for (a) growth 11 and (b) growth 16.*

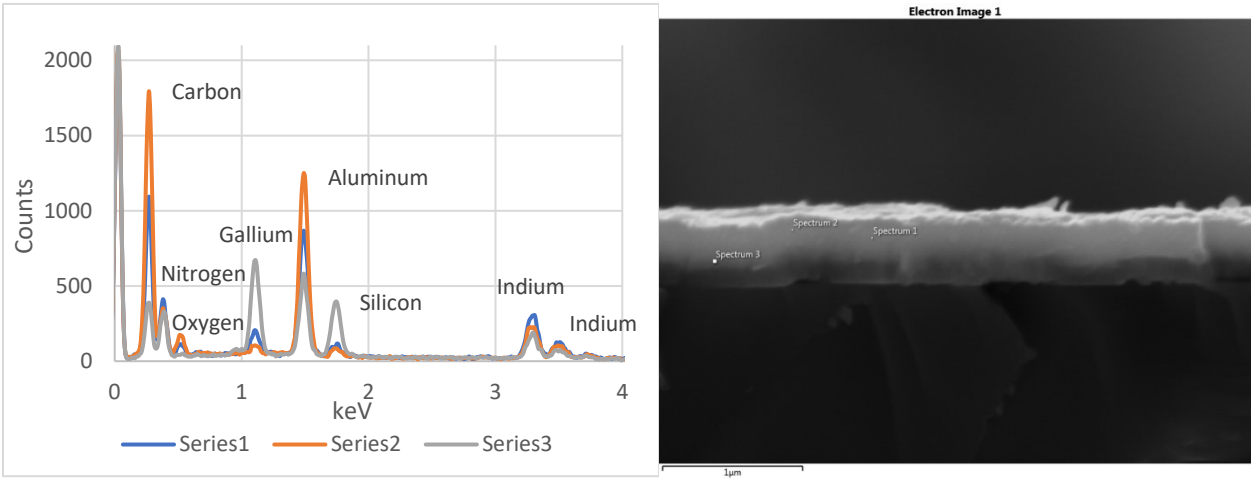


*Figure 35 EDX and corresponding SEM image for growth 11.*

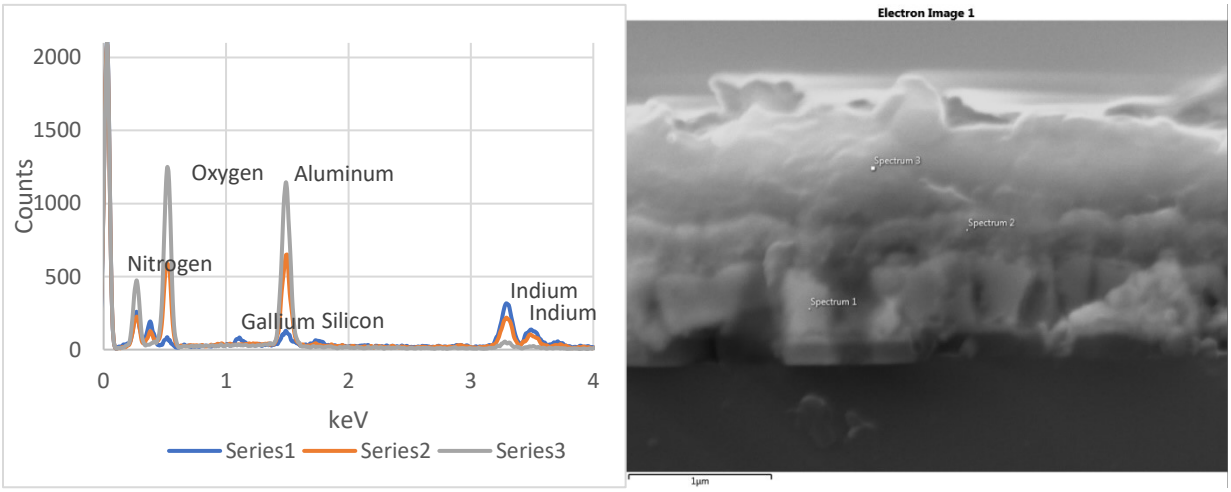


*Figure 36 EDX and corresponding SEM image for growth 16.*

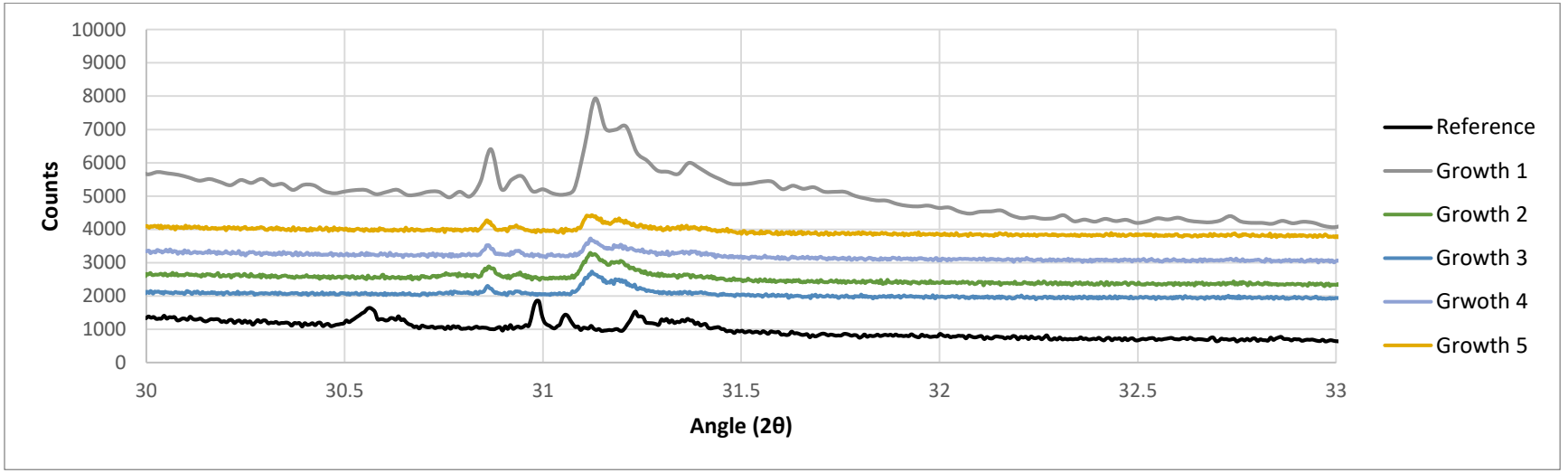


*Figure 37 XRD scans of InN*

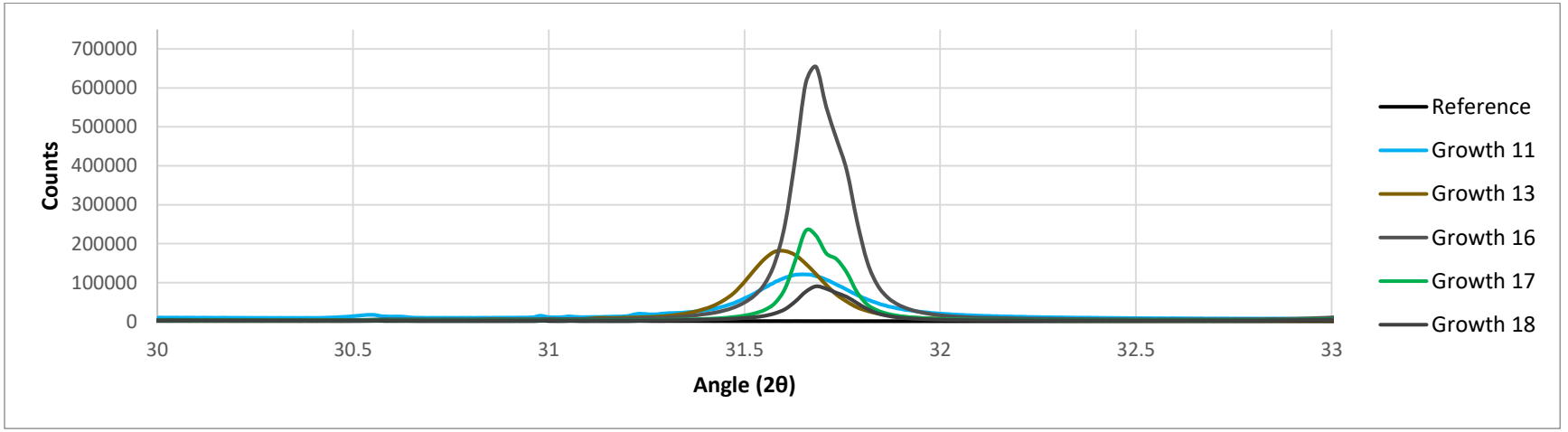


*Figure 38 XRD scans on InAlN*

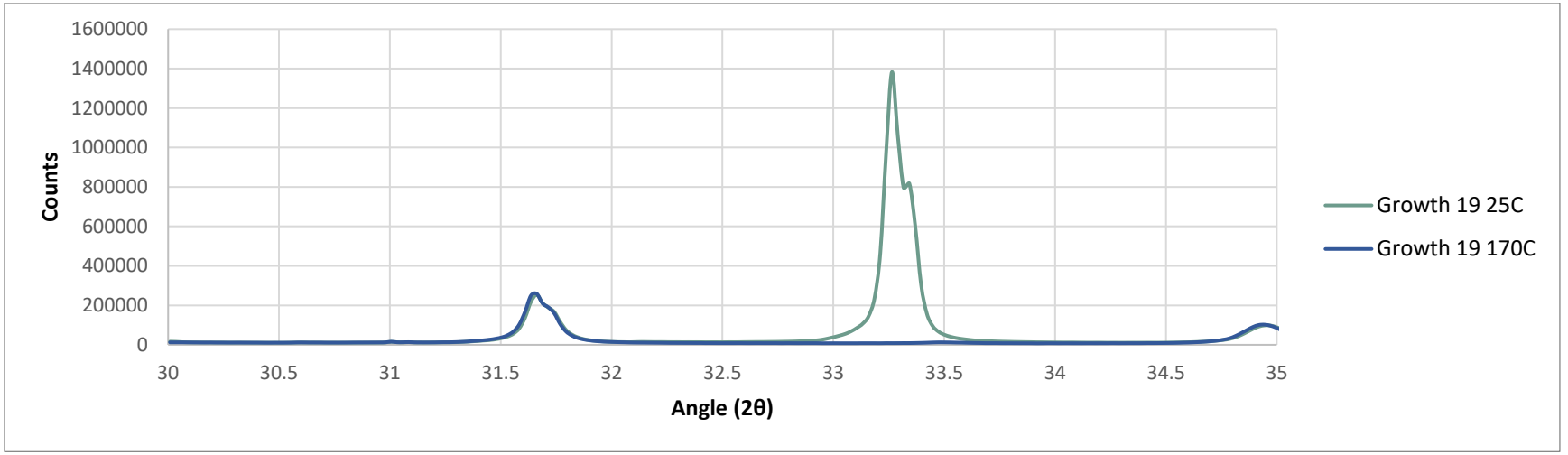


*Figure 39 XRD scan of growth 19 at room temperature and at 170°C*

*Table 18 InN growth parameters*

| Growth Number | MO Ratio | Plasma Type | Plasma power (W) | Plasma Pressure (mTorr) | Temperature | RPM | Cycles | Nitridation Time (s) | Nitridation Power | Technique |
|---|---|---|---|---|---|---|---|---|---|---|
| **1** | 0.1 | RF | 600 | 750 | 540 | 30 | 300 | 300 | 100 | ALD |
| **2** | 0.8 | RF | 300 | 100 | 540 | 60 | 400 | 60 | 300 | Metal Modulated |
| **3** | 0.5 | RF | 200 | 70 | 540 | 60 | 400 | 60 | 200 | Metal Modulated |
| **4** | 0.2 | RF | 200 | 70 | 540 | 60 | 400 | 60 | 200 | Metal Modulated |
| **5** | 0.33 | RF | 200 | 70 | 540 | 60 | 400 | 30 | 200 | Metal Modulated |

*Table 19 InAlN growth parameters*

| Growth Number | Al MO Ratio | In MO Ratio | %In/Al | Plasma Type | Plasma Power (W) | Plasma Pressure (mTorr) | Temperature | RPM | Cycles | Nitridation Time (s) | Nitridation Power (W) | Buffer Layer | Buffer Layer Cycles |
|---|---|---|---|---|---|---|---|---|---|---|---|---|---|
| **6** | 1 | 0.8 | 50/50 | RF | 600 | 300 | 460 | 60 | 210 | 60 | 600 | NA | NA |
| **7** | 1 | 0.8 | 75/25 | RF | 600 | 300 | 460 | 60 | 400 | 60 | 600 | InN | 100 |
| **8** | 1 | 0.8 | 50/50 | RF | 600 | 300 | 460 | 60 | 400 | 60 | 600 | InN | 100 |
| **9** | 1 | 0.8 | 25/75 | RF | 600 | 300 | 460 | 60 | 400 | 60 | 600 | InN | 100 |
| **10** | 1 | 0.8 | 50/50 | RF | 600 | 300 | 460 | 60 | 400 | 60 | 600 | InN | 40 |
| **11** | 1 | 0.8 | 50/50 | RF | 600 | 300 | 460 | 60 | 400 | 60 | 600 | InN | 200 |
| **12** | 1 | 0.8 | 50/50 | RF | 600 | 300 | 460 | 60 | 400 | 60 | 600 | NA | NA |
| **13** | 1 | 0.8 | 50/50 | RF | 600 | 300 | 460 | 60 | 400 | 60 | 600 | InN | 200 |
| **14** | 1 | 0.8 | 50/50 | RF | 600 | 300 | 520 | 60 | 400 | 60 | 600 | InN | 200 |
| **15** | 1 | 0.8 | 50/50 | RF | 600 | 300 | 520 | 60 | 400 | 60 | 600 | InN | 200 |
| **16** | 1 | 1 | 50/50 | RF | 600 | 500 | 540 | 60 | 400 | 60 | 100 | InN | 400 |
| **17** | 1 | 1 | 50/50 | RF | 600 | 500 | 540 | 60 | 400 | 60 | 100 | InN | 400 |
| **18** | 1 | 0.8 | 50/50 | RF | 600 | 500 | 540 | 60 | 400 | 60 | 100 | InN | 400 |
| **19** | 1 | 1 | 50/50 | RF | 600 | 500 | 540 | 60 | 400 | 60 | 100 | InN | 400 |

# Chapter 6 Theoretical Band Structure Calculations

## 6.1 Overview

This chapter covers a theoretical investigation of carbon impurities within InN using an LCAO technique. The resulting bandgap from varying the carbon impurity is also discussed.

## 6.2 Electronic Band Structure of a Generic Crystal

The multinary cell of a compound $A_xB_{1-X}C$ crystal is considered a large primitive supercell which satisfies certain conditions of spatial periodicity to be considered smaller elemental cells. The electronic band structure can be determined by electron interactions within the primitive supercell. The fundamental concept is that the electron band structure of the multinary cell contains the same subbands as the supercell without the localized interactions, which is the sum of the constituting elementary cell band structure. Each cell is also symmetrical to the primitive crystals of AC and BC if the cation and anion positions have no consideration for the nature of their atoms. So, the elementary cell for a binary crystal would be the primitive cell.

For visualization the role of carbon impurities in InN, quasi elementary cells are created with a composition of $InC_xN_{1-x}$. Each of the primitive cells are created by varying the x parameter from 0 to 1 in 0.25 steps, staring with pure InC and replacing anionic carbon with nitrogen until pure InN is reached.

## 6.3 Mathematical Formalism

The number of atomic orbitals in the elementary cell is equal to $n$. For the sake of simplicity, the number of elementary cells in the primitive supercell in each direction of the crystal axis is odd ($N_1 = N_2 = N_3 = 2N + 1$) where $N > 0$). This means that to decompose the band structure transitions between AC and BC, the primitive supercells may only have and odd number of

constituent elementary cells. Only the interactions between the orbitals belonging to a single supercell of the multinary crystal will be used. With is approximation, the electron wave function can be expressed in LCAO terms by:

$$\psi_p(r) = \sum_v \sum_q \sum_g C(p)_{v,q,g} \chi_g^{uq} \quad (12)$$

Where:

$p = p_i$ and $q = q_i$ where $i = 1,2,3$ ... which run over -N…0…N

*r* is the radius vector of the electron

$\sum_v$ is the sum of all the supercells in the crystal

$\sum_g$ is the sum over all the *n* orbitals belonging to the cell

$\sum_q$ is shorthand notation for $\sum_{q_1=-N}^{N} \sum_{q_2=-N}^{N} \sum_{q_3=-N}^{N}$

$\chi_g^{vq} = \chi_g(r - R_q - r_g)$ is the *g*th atomic orbital corresponding to an atom have position vector $r_g$ in the elementary cell characterized by vector $R_q = q_1 a_1 + q_2 a_2 + q_3 a_3$, where $a_1, a_2$ and $a_3$ are the three basis vectors of the primitive supercell defined by the elementary cell. Since only the interactions between the orbitals belonging to the primitive super cell will be considered, only the electron orbital $\varphi_p(r)$ belonging to the primitive supercell shall be used. In a one electron approximation applied to the supercell the orbital becomes:

$$\varphi_p(r) = \sum_q \sum_g C(p)_{g,q} \chi_g^q \quad (13)$$

The expectation of the electron energy is

$$\varepsilon(p) = \langle \varphi_p | \hat{H} | \varphi_p \rangle / \langle \varphi_p | \varphi_p \rangle \quad (14)$$

Where $\hat{H}$ is the Hamiltonian. A Ritz variation procedure done on (14) can be preformed for the coefficients in (13) and the result is a matrix equation for the supercell.

$$HC(p) = \varepsilon(p)SC(p) \quad (15)$$

A hyper matrix of dimension $n(2N+1)^3$ has submatrices $H_{p,q}$ of dimension n and the overlap hyper matrix S has submatrices $S_{p,q}$. to conform with the translational symmetry of the primitive supercell and the Born-con Karman boundary conditions, matrices H and S are cyclic hyper matrices (the transformation of both matrices are similar and only H will be given). The unitary matrix $U$ of dimension $n(2N+1)^3$ having $n \times n$ blocks defined as

$$H'(p) = \sum_q e^{\frac{2\pi ip.q}{2N+1}}\mathbf{1} \quad (16)$$

Will transform H and S in block-diagonal forms (**1** is the unit matrix having dimensions $n \times n$):

$$H' = U^+HU \quad (17)$$

(16) proves that $U^+U = \mathbf{1}$, where the unit matrix **1** has dimensions $n(2N+1)^3$. The *p*th diagonal block of matrix (17) has the form

$$H'(p) = \sum_q e^{\frac{2\pi ip.q}{2N+1}}H(q) \quad (18)$$

Where matrix H(q) is a submatrix of H before the unitary transformation. This submatrix corresponds to the elementary cell having a radius-vector $R_q$. (15) can be multiplied on the LHS by $U^+$and the unit matrix can be inserted in both sides of the equation.

$$U^+HUU^+C(p) = \varepsilon(p)U^+SUU^+C(p) \quad (19)$$

$U^+C(p)$ can be defined by matrix $G(p)$ and by substitution of (17), (19) can be rewritten as

$$H'G(p) = \varepsilon(p)S'G(p) \quad (20)$$

However, $H'$and $S'$ are block diagonal and can be decomposed into a simpler equation

$$H'(p)g(p) = \varepsilon(p)S'(p)g(p) \quad (21)$$

Since the primitive supercell of the multinary crystal is very large, it can be considered that the $N$ number of the elementary cells belonging to a primitive supercell is large as well. Under this consideration, the electron wave vector can be defined as

$$k = k_1 b_1 + k_2 b_2 + k_3 b_3 \quad (22)$$

Where $b_1, b_2$ and $b_3$ are the base vectors of the reciprocal elementary lattice cell and

$$k_j = \frac{2\pi p_j}{[a_j(2N+1)]} \; where \; j = 1, 2, 3 \quad (23)$$

From here, (21) can be rewritten as

$$H(k)g(k) = \varepsilon(k)S(k)g(k) \quad (24)$$

Where

$$H(k) = \sum_q e^{ik.R_q} H(q) \quad (25)$$

The electron band structure of the multinary crystal can be found from (24) as eigenvalues of the matrix $H(k)$. According to (25), every eigenvalue of $H(k)$ contains the corresponding eigenvalues of the matrix $H(q)$ and the electron energy is

$$E(k) = \sum_q e^{ik.R_q} E(q) \quad (26)$$

(26) shows that the electron energy in the multinary crystal is E(k) can be defined as a set of energies E(q). Each element E(q) of this set is an electron energy in the elementary cell having radius $R_q$.

A Fourier transform is taken from both sides of (26) and the dependence of the electron energy on the coordinates will be found

$$E(k) = F[E(k)] = \sum_q \delta(r - R_q)E(q) \quad (27)$$

Where $\delta(r - R_q)$ is the delta function. (27) shows that the electron energy depends on the electron radius vector which depends on the elementary cell.

## 6.4 Interstitial Carbon Impurity States

Carbon is a common contaminant in MOCVD. The carbon atom is inherent in the trimethyl ligand, and it is known from growths of GaAs that appreciable amounts of carbon can be incorporated into the layer. [2] In a typical MOCVD reactor hydrogen is used as a carrier gas and can react with the methyl group to form methane as an exhaust gas. This is not the case in the Lakehead reactor, which uses $N_2$ as the carrier gas, which in turn, leads to an excess of carbon in the system which can interact with the InN layer. Finally, hydrogen is also know to contaminate InN and act like a shallow donor.[45], [46]

## 6.3 Electron Band Structures of $InC_xN_{1-x}$

Electron band structures using an LCAO technique for wurtzite $InC_xN_{1-x}$ for points Γ were calculated by the methods shown above. The calculation shows that for the inter-band electron transitions for the compound alloy, parts of the LCAO electron band structure can be taken corresponding to the configurations of the quasi-elementary cells giving the best combination of deep energy pockets for both electrons in the conduction band and holes in the valence band. Five different types of wurtzite quasi-elementary cells are used and labeled as follows:

1) InC quasi-elementary cell with 2 carbon atoms and 2 indium atoms which corresponds to pure InC.
2) InNC quasi-elementary cell with 1.5 carbon atoms, 0.5 nitrogen atoms and 2 indium atoms ($InC_{0.75}N_{0.25}$).

3) InNC quasi-elementary cell with 1 carbon atom, 1 nitrogen atom and 2 indium atoms ($InC_{0.5}N_{0.5}$).
4) InNC quasi-elementary cell with 0.5 carbon atoms, 1.5 nitrogen atoms and 2 indium atoms ($InC_{0.25}N_{0.75}$).
5) InN quasi-elementary cell with 2 nitrogen atoms and 2 indium atoms which corresponds to pure InN.

The band structure calculations are outlined above and fully explained in [47], MATLAB software has been used for all calculations. Figure 40 shows the calculated band structure for the quasi-elementary cell. Each sector corresponds to the list above. The energy levels $\Gamma_c^n$ and $\Gamma_v^n$ are determined by taking the vacuum energy as 0. The difference between $\Gamma_c^n$ and $\Gamma_v^n$ gives the band gap for each *n* sector which is summarized in Table 20.

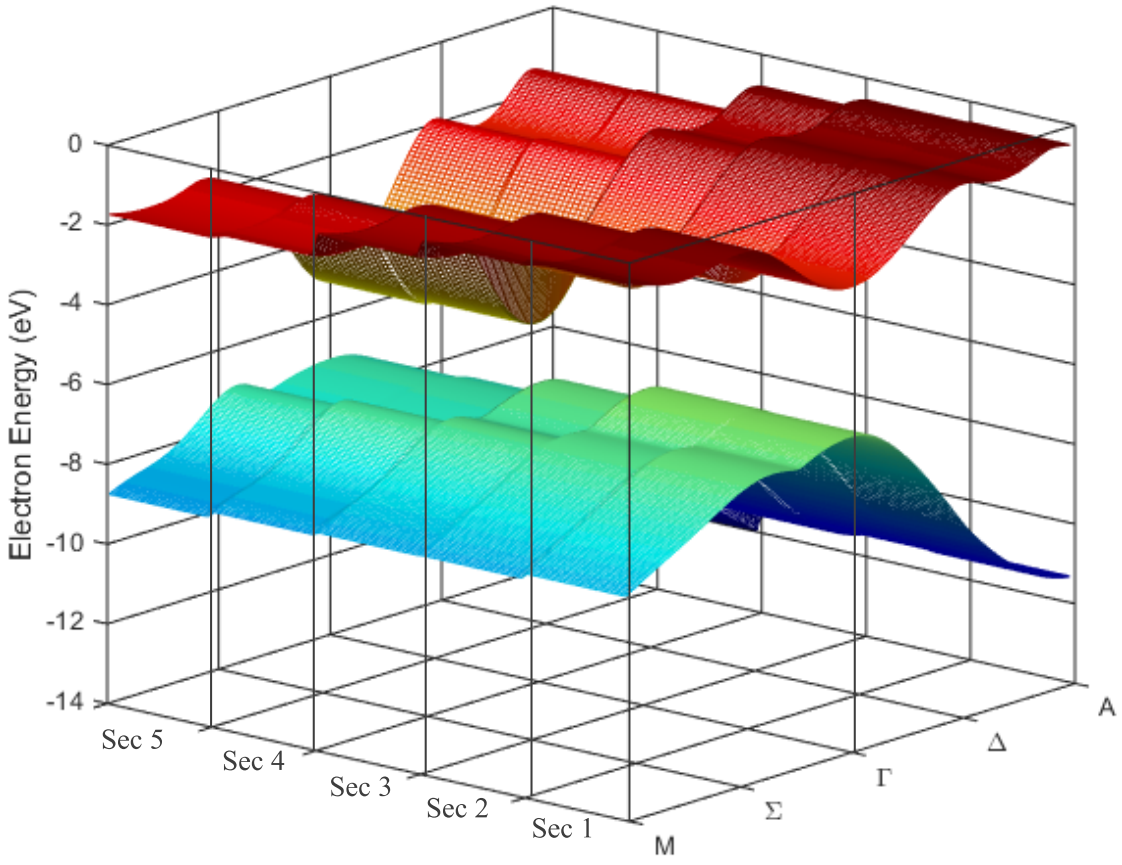


*Figure 40 Calculated band structure of $InC_xN_{1-x}$.*

*Table 20 Conduction, valence and bandgap energies of the quasi-elementary cells*

| Sector | $E_c$ | $E_v$ | $E_g$ |
|---|---|---|---|
| 1 | -2.3854 | -6.1343 | 3.7489 |
| 2 | -2.8142 | -6.0954 | 3.2812 |
| 3 | -3.5409 | -6.5114 | 2.9705 |
| 4 | -5.0431 | -7.0858 | 2.0427 |
| 5 | -5.1254 | -7.1018 | 1.9764 |

The corresponding band diagrams at point Γ is illustrated in Figure 41

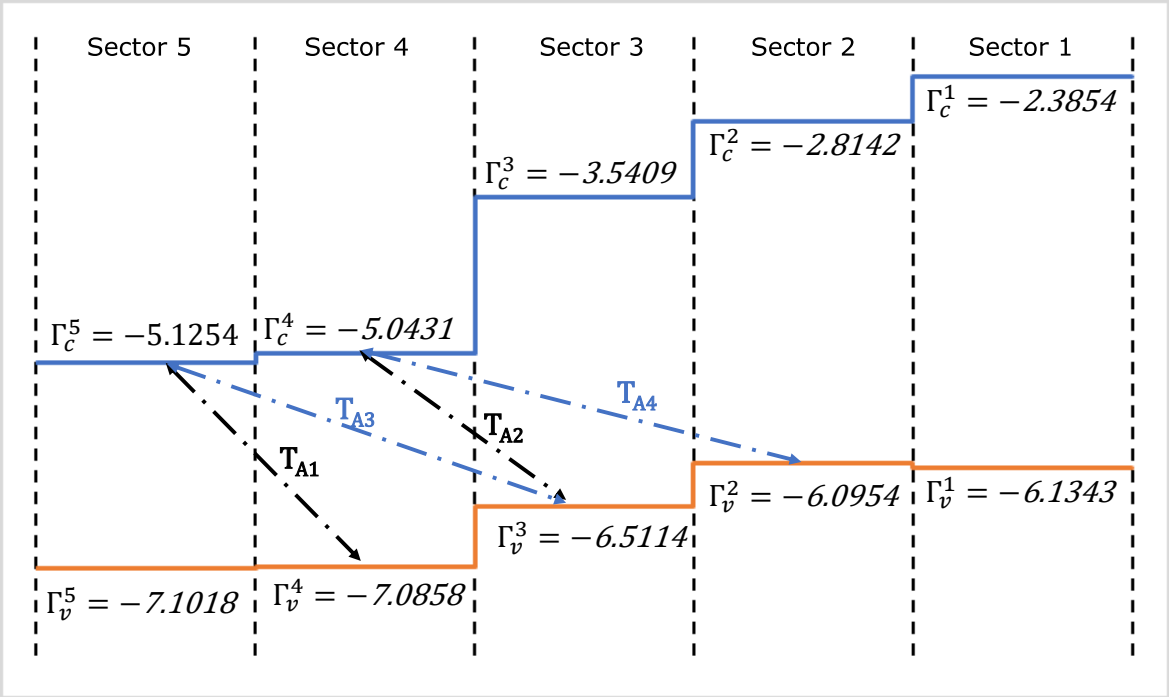


*Figure 41 Electron Band Diagram for $InC_xN_{1-x}$ at point Γ.*

The important features from Figure 40 are the two pockets of energy in the valence band across all compositions. This would indicate a possibility of holes in the valence band with two different effective masses, leading to holes with different levels of mobility within the structure.

In Figure 41, the tunnel optical absorption between $T_{A1}$ ($\Gamma_c^5$ and $\Gamma_v^4$), $T_{A2}$ ($\Gamma_c^4$ and $\Gamma_v^3$), $T_{A3}$ ($\Gamma_c^5$ and $\Gamma_v^3$), and $T_{A4}$ ($\Gamma_c^4$ and $\Gamma_v^2$) has a $E_g$ of 1.4677 eV, 1.86 eV, 1.0523 eV and 1.286 eV respectively.$T_{A1}$ and $T_{A2}$ are primary absorption being nearest neighbours for the tunnelling edge and thus more likely to have tunnelling effects, while $T_{A3}$ and $T_{A4}$ are secondary and less likely to tunnel. However, $T_{A1}$ and $T_{A2}$ have optical bandgaps that have historically been associated with InN, which means that carbon contamination could have been the source of the long-standing confusion with the bandgap of InN.

# Chapter 7 Conclusions

Growths of III-Nitrides using low temperature remote plasma techniques has been demonstrated and analyzed. SiC as a substrate has proven to be an effective substrate to grown upon due to its low lattice mismatch.

Attempts at growths of AlN has resulted in aluminum oxide formation or amorphous AlN being formed verified by SEM imaged. Although no AlN could be detected by XRD or Raman SEM and EDX images did show a least a layer being formed.

Growths of GaN were successfully demonstrated with both smaller FWHM and higher XRD peaks. As well, SEM imaged showed a grown layer or a thicker homogenous layer from the substrate.

InN growths were not successfully grown on their own, only within the combination of InAlN growths did the (0002) peak of InN appear. Again, the AlN peaks did not appear, but SEM images did show layers of InN being grown. In metal was also seen to be grown and verified using a high temperature XRD.

Theoretical calculations using LCAO has shown that carbon contamination as a source of an optical absorption band phenomenon at 1.4677eV range. This range solves a long-standing confusion around the band gap of InN due to tunnelling effects.

## 7.1 Future Work

Future work involves the optimization of growth conditions, specifically the plasma parameters and the injections ratios of the metal organics. Both DC and RF plasma were investigated but no concise solution was found on which technique was more effective at growth.

Characterization of the plasma will need to be done to determine the amount of atomic nitrogen vs ionic nitrogen and which type of plasma contains the most, and what power and pressure give the most plasma density.

The timings for the metal organic sources also need to be optimized. For growths of GaN very little was done with the ratio between the plasma and injection of MO. Investigations on what ratio is appropriate will need to be done, as well as if there should be any overlap between the injection of MO and the plasma being active.

Development of crystallin AlN and InN single layers will need to be optimized for fabrication of a device to be considered. In addition, AlGaN growths will also need to be preformed to see if the ternary alloy of Al and Ga produces any visible effects. If these layers can be achieved then device application could include GaN/AlGaN HEMTs or GaN/InGaN blue LEDs, the formation of which could be achieved at the Lakehead University reactor and verified using equipment found at Lakehead.

# References


[1] H. Morkoç, *Handbook of Nitride Semiconductors and Devices, Materials Properties, Physics and Growth*. John Wiley & Sons, 2009.

[2] L. Vegard, "Die Konstitution der Mischkristalle und die Raumfüllung der Atome," *Z. Phys.*, vol. 5, pp. 17–26, Jan. 1921.

[3] M. Asif Khan *et al.*, "Cleaved cavity optically pumped InGaN–GaN laser grown on spinel substrates," *Appl. Phys. Lett.*, vol. 69, no. 16, pp. 2418–2420, Oct. 1996.

[4] F. Lecourt *et al.*, "InAlN/GaN HEMTs on Sapphire Substrate With 2.9-W/mm Output Power Density at 18 GHz," *IEEE Electron Device Lett.*, vol. 32, no. 11, pp. 1537–1539, Nov. 2011.

[5] S. Uehara, T. Masamoto, A. Onodera, M. Ueno, O. Shimomura, and K. Takemura, "Equation of state of the rocksalt phase of III–V nitrides to 72 GPa or higher," *J. Phys. Chem. Solids*, vol. 58, no. 12, pp. 2093–2099, Dec. 1997.

[6] C. R. E. Jr, N. Nepal, J. K. Hite, and M. A. Mastro, "Perspectives on future directions in III-N semiconductor research," *J. Vac. Sci. Technol. A*, vol. 31, no. 5, p. 058501, Sep. 2013.

[7] O. Ambacher *et al.*, "Two dimensional electron gases induced by spontaneous and piezoelectric polarization in undoped and doped AlGaN/GaN heterostructures," *J. Appl. Phys.*, vol. 87, no. 1, pp. 334–344, Dec. 1999.

[8] C. J. Glassbrenner and G. A. Slack, "Thermal Conductivity of Silicon and Germanium from 3K to the Melting Point," *Phys. Rev.*, vol. 134, no. 4A, pp. A1058–A1069, May 1964.

[9] Q. Xia, H. Xia, and A. L. Ruoff, "Pressure-induced rocksalt phase of aluminum nitride: A metastable structure at ambient condition," *J. Appl. Phys.*, vol. 73, no. 12, pp. 8198–8200, Jun. 1993.

[10] P. Perlin, C. Jauberthie-Carillon, J. P. Itie, A. San Miguel, I. Grzegory, and A. Polian, "Raman scattering and x-ray-absorption spectroscopy in gallium nitride under high pressure," *Phys. Rev. B*, vol. 45, no. 1, pp. 83–89, Jan. 1992.

[11] M. Ueno, M. Yoshida, A. Onodera, O. Shimomura, and K. Takemura, "Stability of the wurtzite-type structure under high pressure: GaN and InN," *Phys. Rev. B*, vol. 49, no. 1, pp. 14–21, Jan. 1994.

[12] H. Morkoç and H. Morkoç, *Handbook of Nitride Semiconductors and Devices*. Weinheim : [Chichester: Wiley-VCH ; John Wiley, distributor], 2008.

[13] R. Quay, *Gallium nitride electronics*, vol. 96. Springer Science & Business Media, 2008.

[14] D. R. Lide, Ed., *CRC Handbook of Chemistry and Physics, 90th Edition*, 90 edition. Boca Raton, FLa.: CRC Press, 2009.

[15] J. H. Edgar, *Properties, Processing and Applications of Gallium Nitride and Related Semiconductors*. INSPEC, 1999.

[16] Safa Kasap and Peter Capper, Eds., *Springer Handbook of Electronic and Photonic Materials*, Illustrated. Springer Science+Business Media, Inc., 2006.

[17] A. Bauer, P. Reischauer, J. Kräusslich, N. Schell, W. Matz, and K. Goetz, "Structure refinement of the silicon carbide polytypes 4H and 6H: unambiguous determination of the refinement parameters," *Acta Crystallogr. Sect. A*, vol. 57, no. 1, pp. 60–67, Jan. 2001.

[18] S. Çörekçi, M. K. Öztürk, B. Akaoğlu, M. Çakmak, S. Özçelik, and E. Özbay, "Structural, morphological, and optical properties of AlGaN/GaN heterostructures with AlN buffer and interlayer," *J. Appl. Phys.*, vol. 101, no. 12, p. 123502, Jun. 2007.

[19] O. Kelekci, P. Tasli, S. S. Cetin, M. Kasap, S. Ozcelik, and E. Ozbay, "Investigation of AlInN HEMT structures with different AlGaN buffer layers grown on sapphire substrates by MOCVD," *Curr. Appl. Phys.*, vol. 12, no. 6, pp. 1600–1605, Nov. 2012.

[20] C. S. Gallinat *et al.*, "In-polar InN grown by plasma-assisted molecular beam epitaxy," *Appl. Phys. Lett.*, vol. 89, no. 3, p. 032109, Jul. 2006.

[21] N. Nepal *et al.*, "Epitaxial Growth of Cubic and Hexagonal InN Thin Films via Plasma-Assisted Atomic Layer Epitaxy," *Cryst. Growth Des.*, vol. 13, no. 4, pp. 1485–1490, Apr. 2013.

[22] T. Araki, Y. Saito, T. Yamaguchi, M. Kurouchi, Y. Nanishi, and H. Naoi, "Radio frequency-molecular beam epitaxial growth of InN epitaxial films on (0001) sapphire and their properties," *J.*

*Vac. Sci. Technol. B Microelectron. Nanometer Struct. Process. Meas. Phenom.*, vol. 22, no. 4, pp. 2139–2143, Jul. 2004.
[23] T. L. Tansley and C. P. Foley, "Optical band gap of indium nitride," *J. Appl. Phys.*, vol. 59, no. 9, pp. 3241–3244, May 1986.
[24] M. Bhatnagar and B. J. Baliga, "Comparison of 6H-SiC, 3C-SiC, and Si for power devices," *IEEE Trans. Electron Devices*, vol. 40, no. 3, pp. 645–655, Mar. 1993.
[25] P. G. Neudeck, "Silicon carbide technology," *VLSI Handb.*, vol. 20061800, 2006.
[26] D. G. Zhao, S. J. Xu, M. H. Xie, S. Y. Tong, and H. Yang, "Stress and its effect on optical properties of GaN epilayers grown on Si(111), 6H-SiC(0001), and c-plane sapphire," *Appl. Phys. Lett.*, vol. 83, no. 4, pp. 677–679, Jul. 2003.
[27] J. H. Edgar *et al.*, "Bulk AlN crystal growth: self-seeding and seeding on 6H-SiC substrates," *J. Cryst. Growth*, vol. 246, no. 3, pp. 187–193, Dec. 2002.
[28] M. Losurdo *et al.*, "Characteristics of InN grown on SiC under the In-rich regime by molecular beam heteroepitaxy," *Appl. Phys. Lett.*, vol. 90, no. 1, p. 011910, Jan. 2007.
[29] M. G. Spencer, J. Palmour, and C. Carter, "Substrate and epitaxial issues for SiC power devices," *IEEE Trans. Electron Devices*, vol. 49, no. 5, pp. 940–945, May 2002.
[30] M. A. Moram and M. E. Vickers, "X-ray diffraction of III-nitrides," *Rep. Prog. Phys.*, vol. 72, no. 3, p. 036502, 2009.
[31] Claudionico, distributed under a CC BY-SA 3.0, *Scanning electron microscope*. 2017.
[32] ARTE, distributed under a CC BY-SA 3.0 *Scanning electron microscope*. 2017.
[33] Muso, distributed under a CC BY-SA 3.0, *Energy-dispersive X-ray spectroscopy*. 2017.
[34] M. Kuball, "Raman spectroscopy of GaN, AlGaN and AlN for process and growth monitoring/control," *Surf. Interface Anal.*, vol. 31, no. 10, pp. 987–999, Oct. 2001.
[35] S. M. George, "Atomic Layer Deposition: An Overview," *Chem. Rev.*, vol. 110, no. 1, pp. 111–131, Jan. 2010.
[36] P. Ruterana, M. Albrecht, and J. Neugebauer, Eds., *Nitride semiconductors: handbook on materials and devices*, 1st ed. Weinheim: Wiley-VCH, 2003.
[37] A. C. Jones and M. L. Hitchman, Eds., *Chemical vapour deposition: precursors, processes and applications*. Cambridge, UK: Royal Society of Chemistry, 2009.
[38] "Low Temperature Growth of GaN and AlN on GaAs Utilizing Metalorganics and Hydrazine," *Jpn. J. Appl. Phys.*, vol. 25, no. 12A, p. L945, Dec. 1986.
[39] H. B. Profijt, S. E. Potts, M. C. M. Van de Sanden, and W. M. M. Kessels, "Plasma-assisted atomic layer deposition: Basics, opportunities, and challenges," *J. Vac. Sci. Technol. A*, vol. 29, no. 5, p. 050801, 2011.
[40] "Gallium Nitride Film Growth Using a Plasma Based Migration Enhanced Afterglow Chemical Vapor Deposition System," *Jpn. J. Appl. Phys.*, vol. 51, no. 1S, p. 01AF02, Jan. 2012.
[41] J. A. Bardwell *et al.*, "A simple wet etch for GaN," *J. Electron. Mater.*, vol. 28, no. 10, pp. L24–L26, Oct. 1999.
[42] T. M. A. tahtamouni, J. Li, J. Y. Lin, and H. X. Jiang, "Surfactant effects of gallium on quality of AlN epilayers grown via metal-organic chemical-vapour deposition on SiC substrates," *J. Phys. Appl. Phys.*, vol. 45, no. 28, p. 285103, 2012.
[43] H. Wang *et al.*, "The Effect of AlN Nucleation Temperature on the Growth of AlN Films via Metalorganic Chemical Vapor Deposition," *J. Electron. Mater.*, vol. 41, no. 3, pp. 466–470, Mar. 2012.
[44] Z. X. Bi *et al.*, "The Temperature Dependence of In Desorption during InN Growth and Annealing," *Mater. Sci. Forum*, vol. 475–479, pp. 3717–3720, 2005.
[45] S. Limpijumnong and C. g. Van de Walle, "Passivation and Doping due to Hydrogen in III-Nitrides," *Phys. Status Solidi B*, vol. 228, no. 1, pp. 303–307, Nov. 2001.
[46] R. L. Lichti, Y. G. Celebi, S. F. J. Cox, and E. A. Davis, "Location of the hydrogen donor in InN: evidence from muonium results," *J. Phys. Condens. Matter*, vol. 16, no. 3, p. 325, 2004.

[47] D. Alexandrov, “Excitons of the structure in wurtzite InxGa1−xN and their properties,” *J. Cryst. Growth*, vol. 246, no. 3, pp. 325–340, Dec. 2002.